



**UNIVERSITY OF ÉVORA**

**SCHOOL OF SCIENCE AND TECHNOLOGY**

DEPARTMENT OF PHYSICS

**MPPT study from a solar photovoltaic panel  
according to perturbations induced by shadows**

**Ana Catarina das Neves Foles**

Supervision: Mouhaydine Tlemçani, Ph.D.

Co-supervision: Paulo Manuel Ferrão Canhoto, Ph.D.

**Masters in Solar Energy Engineering**

Dissertation

Évora, 2017





**UNIVERSITY OF ÉVORA**

**SCHOOL OF SCIENCE AND TECHNOLOGY**

**DEPARTMENT OF PHYSICS**

**MPPT study from a solar photovoltaic panel  
according to perturbations induced by shadows**

**Ana Catarina das Neves Foles**

Supervision: Mouhaydine Tlemçani, Ph.D.

Co-supervision: Paulo Manuel Ferrão Canhoto, Ph.D.

**Masters in Solar Energy Engineering**

Dissertation

Évora, 2017



# Abstract

This work addresses the mathematical and physical modelling of photovoltaic cells and modules, in order to obtain the maximum power output under different environmental operation conditions, including the effect of shadow. Firstly, the Bisection, Newton-Raphson and Secant methods were evaluated for obtaining the characteristic curve of photovoltaic cells, based on the single diode five parameters model and using the values of ideal parameters. Subsequently, the Nelder and Mead algorithm was used to determine the five parameters of the model by fitting the characteristic curve to current and voltage measurements, and accounting to the dependence of cell temperature on environmental conditions by coupling this method to a thermal model of the module. Finally, partial shadowing of photovoltaic modules was studied through a laboratorial experiment, to which conditions the MPPT is calculated through the polynomial fitting of power-voltage curve.

## Keywords

Photovoltaic Energy

Simulation

Optimization

MPPT

Shadow effect



# Resumo

## **Estudo do MPPT de um painel fotovoltaico em função de perturbações induzidas por sombras**

Este trabalho consiste na modelação física e matemática de células e módulos fotovoltaicos, com o intuito de obter a sua máxima potência sob diferentes condições de operação, incluído o efeito de sombreamento. Primeiramente, os métodos da Biseção, Newton-Raphson e Secante foram avaliados recorrendo ao modelo de um díodo e cinco parâmetros de forma a obter a curva característica das células fotovoltaicas, com valores de parâmetros ideais. Seguidamente, o algoritmo de Nelder e Mead foi utilizado para determinar os cinco parâmetros do modelo, recorrendo ao ajuste da curva característica com medidas experimentais de corrente e tensão, e a dependência que os parâmetros ambientais têm na obtenção da temperatura da célula, através do acoplamento do algoritmo com um modelo térmico do módulo. Finalmente, foi estudado o sombreamento parcial de módulos fotovoltaicos através de uma experiência laboratorial, na qual o MPPT é calculado por um ajuste de um polinómio à curva potência-tensão.

## Palavras-chave

Energia fotovoltaica

Simulação

Otimização

MPPT

Efeito de sombreamento





## Acknowledgements

This page is devoted to express my gratitude to the people who made this work possible. Firstly, I would like to thank the two pillars who guided me on this journey and who always tried to put me on the right path. I would like to express my appreciation to my supervisor, Professor Mouhaydine Tlemçani, for all the support he gave me in the realization of this work, availability, sharing of knowledge and ideas, keeping my motivation high, giving me good advices, providing me opportunities for the work to advance, and the good person he went during this work. I want to thank to my co-supervisor, Professor Paulo Canhoto, for being more than a co-supervisor, for sharing his knowledge, being patient and always trying to understand my doubts, giving me a lot of good advices, and the opportunity to appreciate the good person he is.

I want to express my gratitude to Professor Mourad Bezzeghoud for giving me the opportunity to go to the AMPSECA Conference 2017, in Agadir, Morocco.

I am grateful to Instituto de Ciências da Terra (ICT) of the University of Évora for the provided materials, which made possible the realization of the laboratory experiments.

To my group of colleagues, my teacher and colleague André Albino, who have always been available to help me and share his knowledge, and to my colleagues Md Tofael Ahmed and Masud Rana Rashel for their fellowship and help.

I wish to express my gratitude to my parents, Rui Foles and Fernanda Foles, for the sacrifice made correspondent to my entire cycle of studies, and for giving me all the support for the accomplishment of this work, helping me keeping motivated through the entire process.

Finally, I wish to express my gratitude to my syster and my brother, Rita e Ricardo, to my boyfriend, Dorin, and to all my friends for the excellent people they are to me, allowing me to don't be afraid of being audacious and for making me a better person each day.



# Contents

<b>Chapter 1 - Introduction .....</b>	<b>1</b>
1.1 Framework .....	1
1.2 Objectives .....	3
1.3 Motivation.....	3
1.4 State of the art .....	5
1.4.1 Solar cell modelling and simulation .....	8
1.4.2 Parameters determination and sensitivity analysis .....	9
1.4.3 Impact of shadow on the power output of photovoltaic cells.....	9
1.5 Structure of the dissertation .....	11
1.6 Notation .....	11
<b>Chapter 2 – Photovoltaic cell modelling .....</b>	<b>13</b>
2.1 Mathematical model formulation.....	13
2.1.1 Single diode model .....	14
2.1.2 Single diode detailed model .....	15
2.1.3 Double diode model .....	16
2.1.4 Considerations on photovoltaic cell models.....	16
2.2 Determination of the characteristic current-voltage curve.....	18
2.2.1 Bisection method (Binary-Search or Bolzano).....	19
2.2.2 Secant method .....	20
2.2.3 Newton-Raphson method .....	21
2.3 Application results .....	22
2.3.1 Bisection method .....	22
2.3.2 Secant method .....	23
2.3.3 Newton Raphson method .....	24

2.4	Coupling Bisection and Newton-Raphson methods .....	25
2.4.1	Application results .....	26
<b>Chapter 3 - Parameters determination using the Nelder and Mead algorithm .....</b>		<b>28</b>
3.1	Determination of the parameters of a module .....	28
3.1.1	The Nelder and Mead algorithm.....	29
3.2	Determination of guess values of the parameters for the initial simplex.....	35
3.3	Application of the Nelder and Mead for the five parameters model based on the available data of a module .....	37
3.3.1	Initial simplex numerical tolerance .....	39
3.3.2	Imposed noise from the initial curve .....	40
3.3.3	Cycle tolerance and stopping criterion .....	41
3.4	Considerations .....	42
<b>Chapter 4 - Nelder and Mead algorithm development and experimental validation.....</b>		<b>43</b>
4.1	Materials and methods .....	43
4.1.1	Data acquisition system .....	44
4.1.2	Function Generator and GPIB devices .....	45
4.1.3	Photovoltaic module and artificial source .....	45
4.1.4	Instrumentation for air temperature and wind speed measurement.....	46
4.1.5	Temperature sensor with digital display.....	46
4.2	Integrated algorithm for determination of cell temperature, model parameters and maximum power output .....	47
4.2.1	Estimation of cell temperature based on measurements.....	48
4.2.2	Thermal model of the photovoltaic module and cell temperature determination .....	48
4.3	Results of the experimental Nelder and Mead algorithm .....	54

4.4	Considerations .....	55
<b>Chapter 5 - MPPT estimation under shadow conditions .....</b>		<b>57</b>
5.1	The concept of shadow and its effects on photovoltaic conversion of a module 57	
5.2	Analysis of characteristic curve under shaded and unshaded conditions .....	58
5.2.1	Materials and methods.....	58
5.2.2	Module 1 and Module 2 in unshaded conditions.....	58
5.2.3	Module 1 and Module 2 under shaded conditions.....	61
5.3	Curve fitting through polynomials.....	65
5.4	Considerations .....	67
<b>Chapter 6 - Conclusions and future work .....</b>		<b>69</b>
<b>Chapter 7 - References.....</b>		<b>71</b>
<b>Chapter 8 - Appendix.....</b>		<b>75</b>



# List of figures

## Chapter 1

<b>Figure 1.1.1</b> - Global horizontal irradiation distribution [ $kWh/m^2$ ] [6].	2
<b>Figure 1.3.1</b> - World energy consumption prediction until 2040 [2].	4
<b>Figure 1.4.1</b> - Illustration of N-type and P-type semiconductors. (a) n-type, with excess of electrons. (b) p-type, with excess of positive holes [7].	5
<b>Figure 1.4.2</b> - Illustration of the photovoltaic materials chart [1].	6

## Chapter 2

<b>Figure 2.2.1</b> - Single diode model equivalent circuit.	14
<b>Figure 2.2.2</b> – Equivalent circuit of single diode model considering both the shunt and series resistances.	15
<b>Figure 2.2.3</b> – Equivalent circuit of the double diode model.	16
<b>Figure 2.2.4</b> – I-V and P-V curves representation, with the relevant current and voltage values.	17
<b>Figure 2.3.1</b> - Bisection method schematic illustration. Adapted from [18].	19
<b>Figure 2.3.2</b> – Bisection method algorithm flowchart.	19
<b>Figure 2.3.3</b> - Secant method schematic illustration. Adapted from [18].	20
<b>Figure 2.3.4</b> - Secant method algorithm flowchart.	20
<b>Figure 2.3.5</b> - Newton-Raphson method schematic illustration. Adapted from [18].	21
<b>Figure 2.3.6</b> - Newton-Raphson algorithm flowchart.	22
<b>Figure 2.4.1</b> - Error of Bisection method cycle, as a function of the number of iterations.	23
<b>Figure 2.5.1</b> – Flowchart for coupling Bisection and Newton Raphson methods.	26
<b>Figure 2.5.2</b> - Results of I-V and P-V curves of the coupling method.	27

## Chapter 3

<b>Figure 3.1.1</b> – Methods to estimate the parameters. Adapted from [17].	29
<b>Figure 3.1.2</b> - Nelder and Mead steps illustration, for a two variables problem.	30

<b>Figure 3.1.3</b> - Flowchart of the Nelder and Mead algorithm.....	33
<b>Figure 3.1.4</b> - Stopping criterion illustration, with a three vertices example. ....	35
<b>Figure 3.2.1</b> - Error function vs. Irradiance [ $\text{W}/\text{m}^2$ ] [26]. ....	36
<b>Figure 3.2.2</b> - Error function vs. Cell temperature [K] [26]. ....	36
<b>Figure 3.2.3</b> - Error function vs. diode ideality factor [26]. ....	36
<b>Figure 3.2.4</b> – Error function vs. shunt resistance [ $\Omega$ ] [26]. ....	36
<b>Figure 3.2.5</b> - Error function vs. diode saturation current [A] [26]. ....	36
<b>Figure 3.3.1</b> – Relative difference between the obtained values with the Nelder and Mead algorithm and NREL values as a function of the initial simplex maximum deviation. ....	39
<b>Figure 3.3.3</b> - Difference between Nelder and Mead results and NREL values, as a function of the noise in the current measurements. ....	40
<b>Figure 3.3.4</b> - Difference between Nelder and Mead results and NREL values, as a function of the tolerance. ....	41

## Chapter 4

<b>Figure 4.1.1</b> – Schematic of the laboratorial experiment. ....	43
<b>Figure 4.2.1</b> – Flowchart of the algorithm for the determination of cell temperature, model parameters and power output at MPP. ....	47
<b>Figure 4.2.2</b> - Cost function as a function of the variation of the cell temperature. ....	48
<b>Figure 4.2.3</b> - Energy balance of a solar photovoltaic module. Adapted from [46]. ....	49
<b>Figure 4.2.4</b> - Thermal network of the solar photovoltaic module studied model, considering convection, radiation and conduction losses. ....	51

## Chapter 5

<b>Figure 5.2.1</b> - Module 1 (a) and Module 2 (b) used in the laboratorial experiments. ....	59
<b>Figure 5.2.2</b> - P-V curve of Module 1, measured under normal irradiation conditions. ....	59
<b>Figure 5.2.3</b> - I-V curve of Module 1, measured under normal irradiation conditions. ....	60
<b>Figure 5.2.4</b> - Module 2 measured P-V curve under normal irradiation conditions. ....	60
<b>Figure 5.2.5</b> - Module 2 measured I-V curve under normal irradiation conditions. ....	60



<b>Figure 5.2.6</b> - Module 1 and Module 2 shaded cells experimental configurations – Cases of shadow 1 and 2.....	61
<b>Figure 5.2.7</b> - I-V curve of the Module 1, case of shadow 1.....	62
<b>Figure 5.2.8</b> - P-V curve of the Module 1, case of shadow 1.....	62
<b>Figure 5.2.9</b> - I-V curve of the Module 1, case of shadow 2.....	62
<b>Figure 5.2.10</b> - I-V curve of the Module 1, case of shadow 2.....	63
<b>Figure 5.2.11</b> - I-V curve of module 2, case of shadow 1.....	63
<b>Figure 5.2.12</b> - P-V curve of module 2, case of shadow 1.....	64
<b>Figure 5.2.13</b> - I-V curve of module 2, case of shadow 2.....	64
<b>Figure 5.2.14</b> - P-V curve of module 2, case of shadow 2.....	64
<b>Figure 5.3.1</b> - Fifth polynomial fitting with the P-V curve of module 1, case of shadow 1.....	66
<b>Figure 5.3.2</b> - Fifth polynomial fitting with the P-V curve of module 1, case of shadow 2.....	66
<b>Figure 5.3.3</b> - Eighth polynomial fitting with the P-V curve of module 2, case of shadow 1....	67
<b>Figure 5.3.4</b> - Eighth polynomial fitting with the P-V curve of module 2, case of shadow 2....	67



# List of tables

## Chapter 2

<b>Table 2.4.1</b> - Parameters ideal values. ....	22
<b>Table 2.4.2</b> – Secant application results. ....	24
<b>Table 2.4.3</b> - Newton-Raphson application results.....	25
<b>Table 2.5.1</b> – Results with coupled methods. ....	27

## Chapter 3

<b>Table 3.1.1</b> - Steps of the Nelder and Mead algorithm [20]. ....	32
<b>Table 3.3.1</b> – Characteristics of the module Sunrise Solartech SR-M654225 [37]. ....	37
<b>Table 3.3.2</b> - Standard coefficients of the Nelder and Mead algorithm [20]. ....	38
<b>Table 3.3.3</b> – Reference parameters for the Sunrise Solartech SR-M654225 module [37]. ....	38

## Chapter 4

<b>Table 4.1.1</b> – Main measured characteristics of the photovoltaic module.....	45
<b>Table 4.2.1</b> - Initial conditions of the integrated algorithm. ....	55
<b>Table 4.2.2</b> – Results of the estimation of the temperatures, five parameters and maximum power. .....	55

## Chapter 5

<b>Table 5.2.1</b> - Main measured characteristics of the Module 2 (small module). ....	58
<b>Table 5.3.1</b> - Results of the calculated power values on the roots of the polynomials.....	65



# Nomenclature

<b>Simbol</b>	<b>Description</b>	<b>Unit</b>
$A_c$	Area of one cell	$[m^2]$
$A_m$	Area of the module	$[m^2]$
$A_r$	Half of the laboratorial wall area	$[m^2]$
$a, a_k, a_{k+1}$	Value of parameter $a$ during iterative process	—
$b, b_k, b_{k+1}$	Value of parameter $b$ during iterative process	—
$C_n$	Curve coefficients	—
$e_i$	Bases of a vector	—
$e_k$	Errors associated with a succession of values	—
$E(I)$	Error function value	—
$f_b$	Objective function value of the highest vertex	—
$f_w$	Objective function value of the lowest vertex	—
$Gr$	Number of Grashof	—
$G_t$	Irradiance	$[W/m^2]$
$h_{cond,b}$	Conduction heat transfer coefficient of backsheet	$[W/m^2K]$
$h_{cond,g}$	Conduction heat transfer coefficient of glass	$[W/m^2K]$
$h_{conv,b-a}$	Convection heat transfer coefficient from backsheet to air	$[W/m^2K]$
$h_{conv,g-a}$	Convection heat transfer coefficient from glass to air	$[W/m^2K]$
$h_{rad,b-a}$	Radiation heat transfer coefficient from backsheet to air	$[W/m^2K]$
$h_{rad,g-a}$	Radiation heat transfer coefficient from glass to air	$[W/m^2K]$
$I$	Net current	$[A]$
$I_D$	Current in the diode	$[A]$
$I_{err}$	Current output with error	$[A]$
$I_{mp}$	Maximum power point current	$[A]$
$I_{ph}$	Photo-generated current of the cell	$[A]$
$I_s$	Reverse saturation current of the cell	$[A]$
$I_{sc}$	Short circuit current	$[A]$
$I_{std}$	Current standard output	$[A]$
$I_{s1}$	Dark saturation current of the first diode modelling the diffusion current component of the cell	$[A]$
$I_{s2}$	Dark saturation current of the second diode modelling the recombination in the space charge region of the cell	$[A]$
$I_{(p)i}$	Experimental current value	$[A]$

$I_{(\hat{p})i}$	Estimated current value	[A]
$k$	Boltzmann's gas constant	[J/K]
$k_{air}$	Thermal conductivity of the air	[W/mK]
$k_b$	Thermal conductivity of the backsheet	[W/mK]
$k_g$	Thermal conductivity of the glass	[W/mK]
$L$	Length of the module	[m]
$n$	Diode ideality factor of the cell	–
$n_b$	Number of bits	–
$n_s$	Number of series connected cells in the module	–
$N_c$	Number of cells in the module	–
$P_{mp}$	Maximum power output	[W]
$Pr$	Prandtl number	–
$q$	Electronic charge	[C]
$Q_{bottom}$	Total heat loss of the module, from the cell to the backsheet	[W]
$Q_{top}$	Total heat loss of the module, from the cells to the glass	[W]
$Ra$	Rayleigh number	–
$R_{conduction}$	Thermal resistance for conduction heat transfer	[m <sup>2</sup> K/W]
$R_{convection}$	Thermal resistance for convection heat transfer	[m <sup>2</sup> K/W]
$R_{equivalent}$	Thermal resistance for the equivalent heat transfer	[m <sup>2</sup> K/W]
$R_{radiation}$	Thermal resistance for radiation heat transfer	[m <sup>2</sup> K/W]
$R_s$	Internal series resistance of the cell	[Ω]
$R_{sh}$	Shunt resistance of the cell	[Ω]
$S$	Interval	–
$S_f$	Objective function	–
$S_k$	Subinterval	–
$T_a$	Temperature of the ambient air	[K]
$T_b$	Temperature of the backsheet	[K]
$T_c$	Temperature of the cell	[K]
$T_{film_{b-a}}$	Average temperature between the backsheet and the air	[K]
$T_{film_{g-a}}$	Average temperature between the glass and the air	[K]
$T_g$	Temperature of the glass of the module	[K]
$U_L$	Overall heat transfer coefficient	[W/m <sup>2</sup> K]
$v$	Wind speed	[m/s]

$v_c$	Kinetic viscosity of air	$[m^2/s]$
$V$	Voltage imposed across the cell	$[V]$
$V_{mp}$	Maximum power point voltage	$[V]$
$V_{oc}$	Open circuit voltage	$[V]$
$V_t$	P-n junction thermal voltage	$[V]$
$x_C$	Simplex vector where function gets the contracted value	—
$x_E$	Simplex vector where function gets the expanded value	—
$x_k$	Secant and Newton-Raphson methods initial condition	—
$x_{k+1}$	Bisection, Secant and Newton-Raphson iterations values	—
$x_{k-1}$	Secant method initial condition value	—
$x_{min}$	Vertex who corresponds to the lowest function value	—
$x_{max}$	Vertex who corresponds to the highest function value	—
$x_R$	Simplex vertex where function gets the reflected value	—
$x_0$	Centroid of all vertices, except the highest value vertex calculated in the function	—
$x_1 \dots x_6$	Simplex vertices	—

## Greek symbols

$\alpha$	Reflection coefficient	—
$\alpha_s$	Silicon absorptivity	—
$\beta$	Volumetric expansion coefficient	$[K^{-1}]$
$\gamma$	Expansion coefficient	—
$\varepsilon_b$	Backsheet emissivity	—
$\varepsilon_g$	Glass emissivity	—
$\varepsilon_r$	Laboratory room combined emissivity	—
$\eta_e$	Electric power efficiency	$[\%]$
$\rho$	Contraction coefficient	—
$\sigma$	Shrinkage coefficient	—
$\sigma_b$	Stefan-Boltzmann constant	$[W/m^2K^4]$
$\tau$	Glass transmissivity	—
$\Delta x_b$	Backsheet thickness	$[m]$
$\Delta x_g$	Glass thickness	$[m]$

## Acronyms list

AC	Alternating current.
DAQ	Data acquisition board.
DC	Direct current.
GPIB	General-Purpose Interface of Bus.
MPP	Maximum power point.
MPPT	Maximum power point tracking.
NOCT	Nominal Operating Cell Temperature.
NREL	National Renewable Energy Laboratory.
SAM	System Advisor Model.
STC	Standard Test Conditions.
USB	Universal Serial Bus.

## List of communications

This work led to the realization of three oral contributions. The first contribution was related to the first part of this work, which corresponded to the photovoltaic cell modelling, and happened in the University of Évora, in the WES Conference, organized by the Instituto de Ciências da Terra (ICT) (1). The second part of this work, which is related with the five parameters determination based on the one diode model, was presented in the AMPSECA Conference 2017, which took place in Agadir, Morocco (2), and also in the Workshop “Como fazer um artigo científico?”, organized by the ECT, presented in the University of Évora (3).

(1) Foles, A. Albino e M. Tlemçani, “Convergence speed optimization of iterative methods for a Photovoltaic Cell simulation”, in WES Conference, University of Évora, Portugal, 2016.

(2) C. Foles, A. Albino e M. Tlemçani, “Real time characterization of a photovoltaic panel using the five parameters model,” em AMPSECA 2017, Agadir, Morocco, 2017.

(3) C. Foles, A. M. Tlemçani. “Real time characterization of a photovoltaic module considering the single diode five parameters model”, em “Workshop: Como fazer um artigo científico?”, ECT of the University of Évora, Portugal, 2017.



# Chapter 1

## Introduction

Current chapter is devoted to a photovoltaic energy overview. The technology state of the art is presented, in order to gather all the literature research made related to this matter. This dissertation main objectives and motivations will be discussed, so the reader can understand the core of this work.

### 1.1 Framework

The impact of electricity expansion was a growing technology, economic and social activities development, from which an extreme dependency on electricity was born. Electricity is currently a utility, and this fact has caused quite a lot of discussion in the recent decades, due to the consequences of its generalized use and mass exploitation of the primary energy resources used for its generation. Energy supply is currently one of the biggest problems that the human development is facing as the world's electricity production is based mainly in the fossil fuels exploitation and the energy consumption is increasing [1, 2]. The intensive use of fossil fuels leads to large greenhouse gases emissions, and thus to a global warming increase, which has consequences such as average sea level increase, extinction of animals and plants and changes on the intensity of rain. In response to this problem, renewable energies technologies have arisen, powered by renewable sources, as the solar energy, wind, biomass and biofuels and sea waves and tides.

The energy could be harnessed to produce electricity [3]. Photovoltaic conversion is one of the most promising technologies, due to the uniform world availability of the solar resource

and to the direct conversion into electric energy [4]. The total worldwide installed capacity of the photovoltaic technology was by the end of 2015 an amounted value of 227.1 GW. Also in 2015, the world's installed photovoltaic capacity reached 50 GW [5]. It is expected that solar photovoltaic will become a serious alternative to fossil fuels in the nearest future. The issues concerning the energy independence, energy security, stability of energy supply and energy sources diversification will become crucial these days [3]. Photovoltaic systems, except for the concentration systems, have the advantage of using not only direct sunlight but also the diffuse component of sunlight, i.e. solar photovoltaic technology produces power even if the sky is not completely clear, which could enable the photovoltaic effective deployment in all the world regions [5]. World irradiation distribution is shown in Figure 1.1.1.

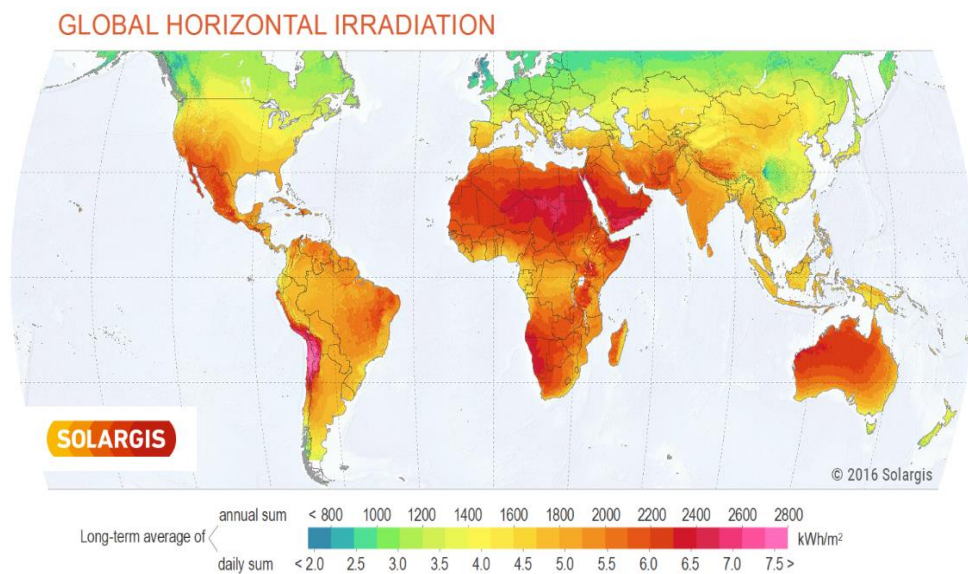


**Figure 1.1.1** - Global horizontal irradiation distribution [ $kWh/m^2$ ] [6].

A solar photovoltaic system is constituted by photovoltaic modules, which are composed of several individual cells electrically connected between each other, and convert solar energy directly into electricity [7].

On one hand, photovoltaic energy generation strongly depends on the atmospheric conditions, via the incident solar irradiance and cell temperature and, on the other hand, there is only one operation point corresponding to the maximum power output [8]. Thus, a maximum power point tracker (MPPT), which makes use of a control circuit or logic that searches for this point, allows the extraction of the maximum power that the module can deliver under each operation conditions. The MPPT is a crucial procedure that deals with those changing

atmospheric conditions [9]. This strategy enables an optimization of the operating voltage to maximize the current [7]. MPPT are most applied in on-grid systems, to optimize the produced energy from the photovoltaic system. A high efficiency DC/DC converter functions as an optimal electrical load for a solar photovoltaic module, converting the power to a voltage or current more suitable than the load connected to these systems. Currently, MPPT cost has been reduced and its use is becoming more common [7].

In general, despite of the scientific and technological improvements and governmental incentives in some countries, the cost of the grid-connected energy is still high and yet not competitive with the fossil fuelled power plants [4].

## 1.2 Objectives

Present dissertation has the main aim of study the effect that some internal and external conditions have in the maximum power point tracking, in solar photovoltaic conversion systems. The construction of physical and mathematical models that simulate those conditions has motivated the world's research with multiple diversified approaches.

Therefore, the aim of this study is divided in three main objectives, being the first the elaboration and validation of the single-diode mathematical model applied to the photovoltaic response characterization, by using numerical iterative methods. Three numerical iterative methods will be studied and compared. This approach has the aim of enabling the estimation of photovoltaic energy generation in a reliable and fast way.

The second objective is the estimation of the five parameters of the single diode model equivalent circuit of the photovoltaic cell. The determination of the parameters is made through the application of an existing and quite robust method, known as the Nelder and Mead algorithm, to a photovoltaic cell and module.

The third and final objective is to estimate the maximum power output of photovoltaics modules in shadow conditions, through a laboratorial procedure.

## 1.3 Motivation

Energy is one of the most crucial factors of economic development and prosperity of countries and society [10]. Growing energy demand is one of the key issues of the 21<sup>st</sup> century [10]. In

[2] is predicted that the world energy consumption will increase 28% between 2015 and 2040, as can be seen in Figure 1.3.1.

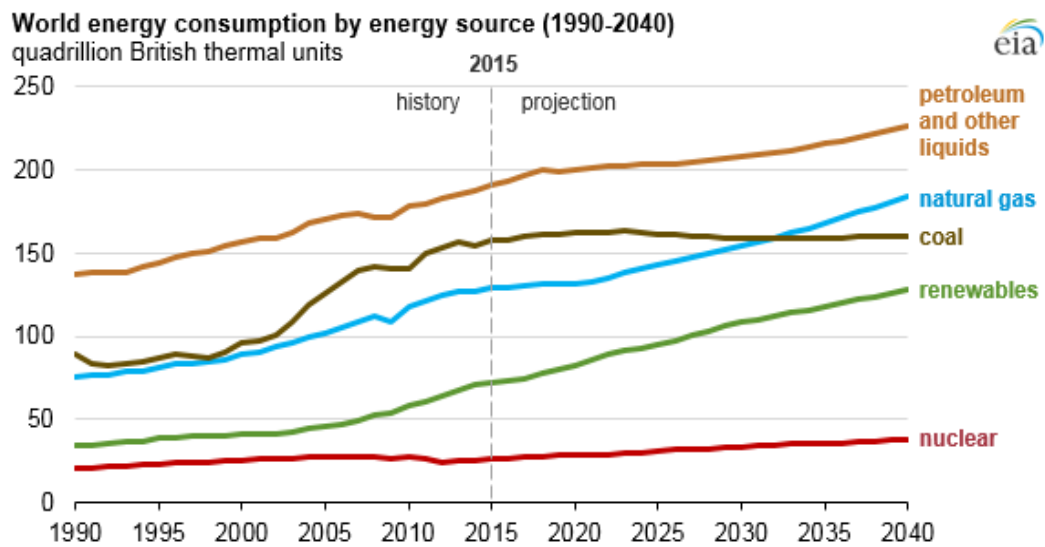


**Figure 1.3.1** - World energy consumption prediction until 2040 [2].

Actual global energy situation is dominated by fossil fuels, which has severe impacts on regional climatic conditions and energy security, and nuclear power plants are directly related with radioactive emissions. The renewable energy technology is more secure, available and pollute less as compared with the conventional sources [10]. Photovoltaic systems provide multiple benefits, such as the fact of being non-polluting devices, needing of few maintenance, long lifetime and in some situations, the technology alone the decentralised generation of energy [4].

Currently, photovoltaic technology development is divided in two key specific areas, with the main aim of increasing the overall conversion efficiency [9]:

- Cell material;
- Power conditioner technology (DC/DC and/or DC/AC converters).

Research is being carried out to advance in the solar cells materials area, such as monocrystalline and polycrystalline silicon cells, amorphous silicon and thin film cells, although their energy conversion efficiency is still low and their cost high [9, 4]. In the case of the power conditioner, the author of [9] defines it as having a very important role in the improvement of power conversion efficiency, and as being a good path to reduce the costs of photovoltaic systems.

The goal of maximizing the power output could be made with the help of power electronics, taking into consideration the variation of the environmental conditions. Optimal operating conditions guarantee is very important to minimize power loses, due to, for example, shadows, dust, debris or dirt accumulations, or system failures. The exploitation of robust algorithms applied to photovoltaic systems is a solution that guarantees achieving the maximum power point output, aiming the development of low cost converters, which is the main motivation of this dissertation.

## 1.4 State of the art

Alexandre Edmond Becquerel discovered the photovoltaic effect in 1839 through exposing selenium material to light, creating voltage across the material. In the following years, the scientists Charles Fritz, Edward Weston, Nikola Tesla and Albert Einstein contributed to the development of this effect [11]. The first application of solar photovoltaic cells was in space, in the year of 1958, where the cost isn't an obstacle [7].

Photovoltaic cells are made of semiconductors, which are average conductors of electricity [7]. Having two semiconductor materials, if one of them is doped and has an excessive of electrons, its called the N-type semiconductor, and the other, which has lack of electrons, its called the P-type semiconductor, as can be observed in Figure 1.4.1, shown below. In the P-N region of a silicon type cell, the free electrons of the N-type silicon occupy the holes of the P-type silicon, creating an electrical field. The photons hit the cell and collide with the electrons of the silicon. Due to the electric field created by the P-N junction, the electrons flow from the P-film to the N-film by an electric conductor, generating electricity [7].

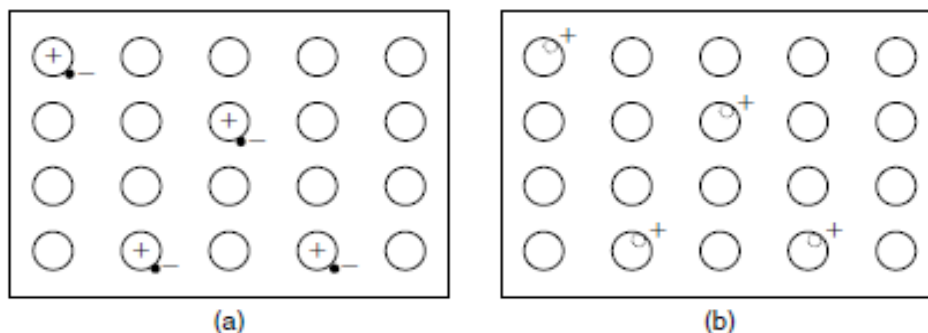


**Figure 1.4.1** - Illustration of N-type and P-type semiconductors. (a) n-type, with excess of electrons. (b) p-type, with excess of positive holes [7].

The most commonly used materials in the solar cells fabrication are the monocrystalline and polycrystalline silicon (Si), cadmium telluride (CdTe), gallium arsenide (GaAs), and triple-junction solar cells, composed of indium gallium phosphide (InGaP) [12].

The cells are commonly divided in first, second and third generation. First generation cells are composed by monocrystalline and polycrystalline cells, which dominate the market on a 90% share, due to its higher efficiency and reliability compared to the other cells technologies [12]. Monocrystalline silicon is characterized by having a more intense process of production (by the Czochralski method, Cz), being more efficient, near 16%, and having a higher cost than the polycrystalline cells, which has an efficiency of 11%. Second generation has approximately a 10% share of the market and its related to the thin films deposition on rigid substrates. Its also characterized by using reduced materials and low energy consumption in the fabrication phase. The amorphous silicon is produced in vacuum through thin films deposition technology, and because the material is unstable its efficiency is about 6%. CIS (CuInSe<sub>2</sub>) have an efficiency of 11%, although face some problems in the fabrication phase. Cadmium telluride (CdTe) cells have low production costs and its efficiencies are near 11%, however these elements are related to issues of contamination and scarcity. Finally, the third-generation cells are still in development, but are already being used in high solar concentration applications. Gallium arsenide (GaAs) is applied in high efficiency cells, reaching nearly 40%, and have a high cost. Tandem cells are used in high solar concentration, combined with Fresnel lenses, with multijunction cells. Organic cells are cells who are composed of organic semiconductors materials, and can set over flexible plastics and films, and could be transparent or have distinct colours (5% efficiency). Materials such as photonics are nanostructured materials who can be introduced in cells, to help in the solar radiation absorption, to increase the respective efficiency [1, 3, 7, 12]. Figure 1.4.2 presents a photovoltaic materials flowchart.

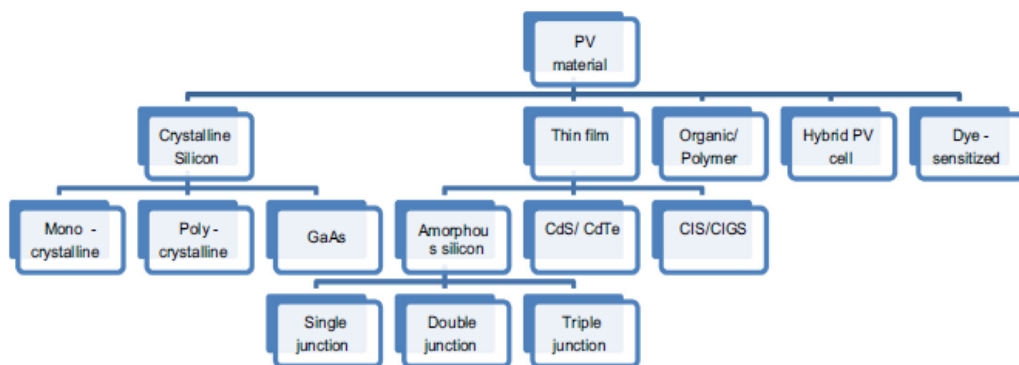


**Figure 1.4.2** - Illustration of the photovoltaic materials chart [1].

Because the cells size is very small, which corresponds to a small power production, solar cells are electrically connected, until the obtained power is the required for the desired application [10]. The degree of purity of the silicon needed to make a photovoltaic cell is high, compared with other electronic devices who use silicon as a component. This is one of the main reasons of the relative high cost of the modules and why electricity from solar photovoltaic systems is more expensive than electricity produced through fossil fuels [12]. However, the decreasing cells price over the past years have been contributing to its world spreading. Their expected lifetime had also increased, until 25 years or more [13]. Currently, research has been focused in developing the materials technology [12].

Photovoltaic systems could be grid-connected with the power grid or off-grid (stand-alone), which means that the installation is independent from the grid. Photovoltaic modules and an inverter, which converts the direct current in alternated current, in conditions of frequency, amplitude and phase of the grid, to inject in the electric grid, constitute the grid-connected systems. Off-grid photovoltaic systems are composed of photovoltaic modules, an inverter, a battery bank and a voltage regulator. Off-grid systems are mainly used in rural areas, far from the grid and where a decentralised energy generation is imposed [7].

Photovoltaic systems are also divided in two subcategories, depending on the existence or not of tracking. In this way, the photovoltaic system could be fixed, and usually facing to the south direction (local meridian), or could have a tracking system, which means that the photovoltaic modules follow the apparent sun trajectory in the sky, and this one could have a single (N-S or E-W) or double axis tracking (N-S and E-W) [10].

Photovoltaic conversion of solar energy has multiple applications such as building integrated photovoltaic (BIPV), transportation, communications, solar roadways, rural electrifications [10], illumination, water pumping, storage charging, desalinization, technologies hibridization and high concentration photovoltaics [7].

DC (direct current) electricity generated through photovoltaic systems can be converted in AC (alternated current) or stored in a battery bank for later use. Technology has supported the growth of renewable energies harvesting. Electronic converters made possible the connection between renewables energy systems and the existing power grid and conventional power plants, improving the energy harvesting through dedicated controls. Photovoltaic systems that are connected to the grid have a power electronics DC/DC converter to ensure the maximum power output with the MPPT, and a DC/AC converter to connect with the grid [13].

In [13] it is showed that the currently research challenges and opportunities are focused in reliability issues of the technology for power generation, medium voltage photovoltaic systems, high-efficiency thin-film cells and electric energy storage from photovoltaic systems. Until 2025 it is expected an improvement and implementation of high voltage photovoltaic systems, to increase its lifetime to 20-30 years and of its inverter, the implementation of micro-inverters, and the reduction of the levelized cost of electricity (LCOE) [13].

The possibility of predicting the response of a photovoltaic power plant due to the variation of incident irradiance, air temperature and load conditions is very important for sizing such systems and converters, as well as for the designing of the MPPT and control strategies [7].

#### 1.4.1 Solar cell modelling and simulation

With the aim of extracting the maximum power from a photovoltaic plant, and with the help of MPPT control techniques, it is crucial to characterize study and model a single photovoltaic cell [14]. A solar cell can be described through an equivalent circuit, with the most used models being the single diode model and the double diode model, which are represented by four or five parameters, as described in [4, 7, 15, 16]. Those models allow the construction of the current-voltage curve (I-V) and of the power-voltage curve (P-V) [7]. These two models are widely known and differ from each other in terms of complexity and their use depends on the type of the application [4, 17]. Since the net electric current of the equivalent circuit is a transcendental function, it is necessary to use iterative methods, in order to obtain the solar cell current-voltage characteristic curve [7, 4]. This fact leads to a deeper study of root-finding iterative methods described in [18], and its application to the photovoltaic cell and module. Some of the numerical methods used for the construction of the I-V and P-V curves are the Bisection method, Newton-Raphson method and Secant method, as explained and presented in the work developed in [19].

The unknown parameters of the solar cell models must be determined for the given type of cell, whose characteristics are to be reproduced by the model. Several approaches for parameters determination can be adopted using the datasheet parameters or measured I-V curves [4].



### 1.4.2 Parameters determination and sensitivity analysis

A solar photovoltaic cell can be described by some points of the characteristic curve, such as the short circuit current, the open circuit voltage and the diode ideality factor [14]. Additionally to those values, the I-V curve could be described by four parameters, including the diode ideality factor,  $n$ : the reverse saturation current of the diode,  $I_s$ , the photo-generated current,  $I_{ph}$ , and the series resistance,  $R_s$ . The shunt resistance,  $R_{sh}$ , is the fifth parameter of the detailed single diode model [4].

Nowadays, these parameters are not available directly from the manufacturers of photovoltaic modules. However, even if they were available from the manufacturers, the parameters of the model vary in time and with the aging of materials or technical faults. This is the main reason to identify these parameters by direct I-V measurements, in real-time [17].

A refined method is needed, in order to obtain a good photovoltaic cell or module characterization. A well-considered choice is to work with the Nelder and Mead algorithm [20], which is a direct search optimization method. In [20, 21, 22, 23] this method is explained and deeply analysed, and its application in the photovoltaic field is presented in [17, 24]. Nelder and Mead algorithm is widely applied to real problems, due to its robustness characteristic in solving optimization problems [24].

In [22] it is explained that the algorithm can converge to local minimums or maximums, although showing a good effectiveness after a few iterations steps. Another important aspect is its performance decreasing with the increase in the number of the parameters [24].

To well estimate the parameters using the Nelder and Mead algorithm it is crucial to understand the parameters response, becoming crucial to make a sensitivity parameters analysis, work developed by the research work in [25, 26].

The analysis of the Nelder and Mead algorithm was study and developed, leading to the presentation of the work in the AMPSECA Conference [27] and in the Workshop of ECT event [28].

### 1.4.3 Impact of shadow on the power output of photovoltaic cells

A shadow could be described as a “darker” region that is formed due to the obstruction of direct irradiance from the sun, caused by the existence of an obstacle between the source of light and shaded space. The shadow changes position according to the origin of light (sun),

and because of that, it varies in time, with environmental conditions and its geometric shape is not constant over time.

The shading of a photovoltaic module is a phenomenon that derives from the module-sun position and the surroundings obstacles. This could happen in any outdoor environment, being that surrounding ambient constituted by trees, passing clouds, high edification [29]. Shadow effect reduces the power output from photovoltaic arrays, which is recognized by the reduction of the energy generation as compared to unshaded arrays in grid-connected photovoltaic systems. The main consequence of shadow is the occurrence of hot spots, which could be avoided by including bypass diodes in the systems. The main consequences of both of those factors are cells damage and power losses [4], which leads to a decrease in performance and lifetime. For example, if a cell from a module is shaded, it will affect all the cell string (series connection of cells) because the current becomes limited. This is the main cause of temperature increase [29]. If the shadow covers partially the module with cells in series connection, the shaded cells work with a reverse bias voltage, to provide the same current as the unshaded ones. This leads to power consumption, due to reverse power polarity, and a power output reduction of the module [30].

A partially shaded module shows a multiple maximum power point, which makes the I-V characteristics analysis more complex. The multiple points present an efficiency decrease in the MPPT search. The consequence is the difficulty of the MPPT algorithm to distinguish the global maximum and the local ones [31].

Shadow identification is currently an emphasis research field. In [29, 30, 32] the single diode model is used, and the partial shadow model derive the different irradiance values, analysing bypass diodes in parallel and series modules connections. In [33] it is proposed a study of a three-diode model, showing best results applied to the industrial scale. In [34] partial shading is studied, with different modules configurations (from three to six modules connection), bypass diodes, number of shaded cells and cells configuration (series or parallel), based on a photovoltaic circuit model on piecewise linear parallel branches (PLPB).

This works focus on getting the maximum possible power from a photovoltaic module, and understanding the shadow effect is extremely important to improve this aspect. One can try to identify shadows through the obtained response from the I-V measurements that constitute the characteristic curve of a single photovoltaic cell or module.

## 1.5 Structure of the dissertation

This dissertation is divided in six major chapters, including this one. Following, it will be presented a brief description of each chapter.

Chapter 2 presents the fundamental concepts that affect the performance of a photovoltaic cell. Thus, the mathematical and physical models of the five and seven parameters that are used to model the cells are deeply analysed. The iterative root-finding methods studied were the Newton-Raphson, Bisection and Secant methods.

Chapter 3 introduces the concepts for a proper parameters estimation of the equivalent circuit, in which the application of the Nelder and Mead algorithm is explained. Subsequently, the algorithm is analysed with other known parameters.

Chapter 4 is dedicated to the study and application of the Nelder and Mead algorithm in order to obtain the five parameters of a cell, with laboratorial experiment validation. Measuring the current and voltage of a module, the best fit of characteristic curve is made, to obtain its parameters. Through the ambient air temperature, glass temperature, solar incident radiation, and wind, the temperature of the cell is estimated, in order to better describe the experimental conditions and correspondent parameters.

Chapter 5 focus on the shadow identification, which consists of understanding the P-V curve under shadow conditions, and calculating the respective MPP.

Chapter 6 presents the main conclusions of this work and the guiding principles to future work.

## 1.6 Notation

This dissertation is written in United Kingdom English and the used references style follows the IEEE 2006 standard, sequentially numbered. The list of symbols and acronyms are presented in the symbols list and acronyms list. The tables and figures captions have the same alphanumeric font size.



# Chapter 2

## Photovoltaic cell modelling

The present chapter addresses the mathematical model formulation of the characteristic current-voltage curve of the photovoltaic cell. The curve will be deeply analysed, based on two main approaches – the single diode model and the double diode model. After this point, the curve will be determined, with the help of three numerical methods, based on the five parameters of the single diode model. The chapter ends with an optimized way of determining the characteristic I-V curve.

### 2.1 Mathematical model formulation

The electric current that is produced when the photons hit the solar cell is often called photo-generated current,  $I_{ph}$ . If there is no solar radiation, the solar cell works as a diode, which means that there is no generation of current neither voltage. On the other side, if the cell is connected to an external voltage supply, a current is generated, the diode current, or dark current [7, 14, 15].

A photovoltaic cell can be described through an equivalent electric circuit [4, 15]. The equivalent circuit models simulate the solar cell response [16]. There are two models based on the modified Shockley diode equation that allow a correct solar cell modelling, namely, the single diode model (referred also as the single exponential model), and the two-diode model (referred also as the double exponential model) [4, 17].

### 2.1.1 Single diode model

The single diode model has four parameters, namely, a constant current source,  $I_{ph}$ , an ideality factor of a diode in parallel and a resistance in series, which accounts for the losses due to the internal resistance of the cell, and of the contacts and interconnections between cells and modules [14, 16]. This model is characterized by its good precision and some authors describe it by the most suitable model for the diagnostics of photovoltaic arrays [4]. The equivalent circuit of this model is shown in Figure 2.2.1.

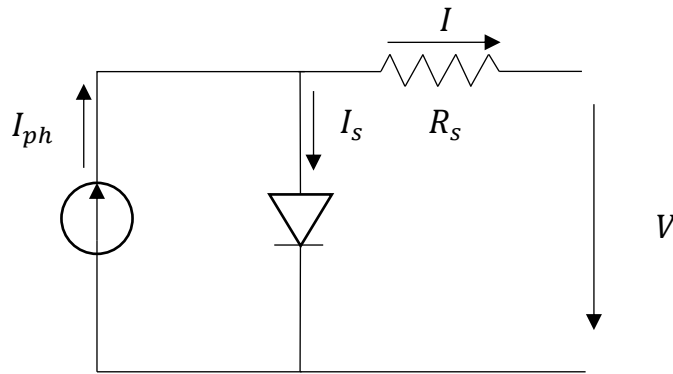


**Figure 2.1.1** - Single diode model equivalent circuit.

The current of the single diode model,  $I$ , is determined by equations (1) and (2),

$$I = I_{ph} - I_D \quad (1)$$

$$I = I_{ph} - I_s \left( e^{\frac{V+IR_s}{V_t}} - 1 \right) \quad (2)$$

Where  $V_t$  is the module thermal voltage, and its expression is

$$V_t = \frac{n_s n k T_c}{q} \quad (3)$$

and where,

$I_{ph}$  - Photo-generated current [A];

$I_s$  - Dark saturation current [A];

$n_s$  - Number of series connected cells in the module;

$n$  - Diode ideality factor;

$k$  – Boltzmann’s gas constant,  $1.381 \times 10^{-23}$  [J/K];

$T$  – Temperature [K];

$q$  – Electronic charge,  $1.602 \times 10^{-19}$  [C];

$R_s$  – Module internal series resistance [ $\Omega$ ];

$V$  – Voltage imposed across the cell [V];

$I$  – Net current [A].

### 2.1.2 Single diode detailed model

The detailed model with single diode has five parameters, further considering a shunt resistance [4, 35], as compared to the simple single diode model. This resistance accounts for “the losses due to the leakage currents across the junction and within the cell due to crystal imperfections and impurities” [4]. Figure 2.2.2 presents the equivalent circuit of this model.

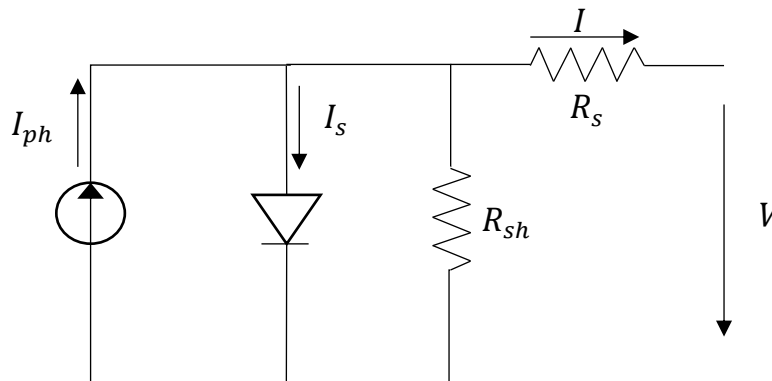


**Figure 2.1.2** – Equivalent circuit of single diode model considering both the shunt and series resistances.

The current of the single diode detailed model,  $I$ , is determined by Eq. (4):

$$I = I_{ph} - I_s \left( e^{\frac{V+IR_s}{V_t}} - 1 \right) - \frac{V + IR_s}{R_{sh}} \quad (4)$$

and where,

$R_{sh}$  - Module Shunt resistance [ $\Omega$ ].

Usually, the shunt resistance is much higher than the load resistance and, by comparison, the series resistance is much lower, so less power is dissipated [7]

### 2.1.3 Double diode model

The double diode model includes another diode in parallel in the equivalent circuit. This diode accounts for “the losses due to the carrier recombination in the space charge region of the junction, and those due to surface recombination”. The first diode is responsible for the component of diffusion current. In this case, an additional parameter is included through the reverse saturation current of the second diode, while the ideality factors are known for both diodes [4]. The equivalent circuit of this model is shown in Figure 2.2.3.

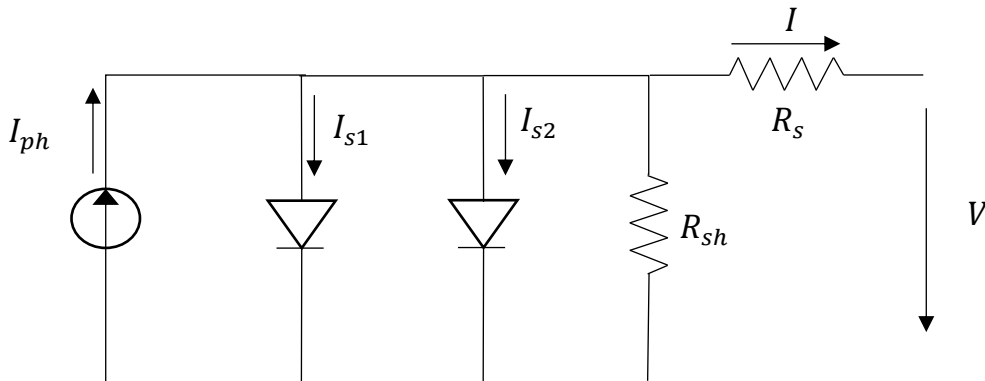


**Figure 2.1.3** – Equivalent circuit of the double diode model.

The current of the double diode model,  $I$ , is determined by equation (5):

$$I = I_{ph} - I_{s1} \left( e^{\frac{V+IR_s}{V_t}} - 1 \right) - I_{s2} \left( e^{\frac{V+IR_s}{2V_t}} - 1 \right) - \frac{V + IR_s}{R_{sh}} \quad (5)$$

and where,

$I_{s1}$  – Dark saturation current of the first diode modelling the diffusion current component [A];

$I_{s2}$  – Dark saturation current of the second diode modelling the recombination in the space charge region [A].

### 2.1.4 Considerations on photovoltaic cell models

In the single diode model, the diode ideality factor accounts for the effect of recombination in the space-charge region. This model is less accurate than the double diode model at lower values of incident irradiance, and can result in negative values of the series resistance. When the irradiance values are higher, this model predicts those values with significant differences, not offering constant results. The double diode model includes the space-charge recombination effect, because “a separate current component with its own exponential



voltage dependence” is modelled. This model is described as being a more accurate description of the solar cell performance than that of the single-diode [16]. The single diode detailed model is sometimes referred to as the five-parameters model [4].

The characteristic curve of a solar cell is the relation between current and voltage, for a certain given irradiance,  $G_t$ , and a cell temperature,  $T_c$ . The convention imposes as positive the current produced by the cell when receives solar radiation, and as positive the voltage that is, in that way, applied to the terminal of the cell. If the cell is short-circuited, the current has its maximum value, and the correspondent voltage is zero. If the circuit is open, the voltage value has its maximum, and the correspondent current is zero. These two points are extremely important to recognise the I-V curve, and between them the power output is higher than zero [7]. Figure 2.2.4 presents the I-V and P-V curves between those points.

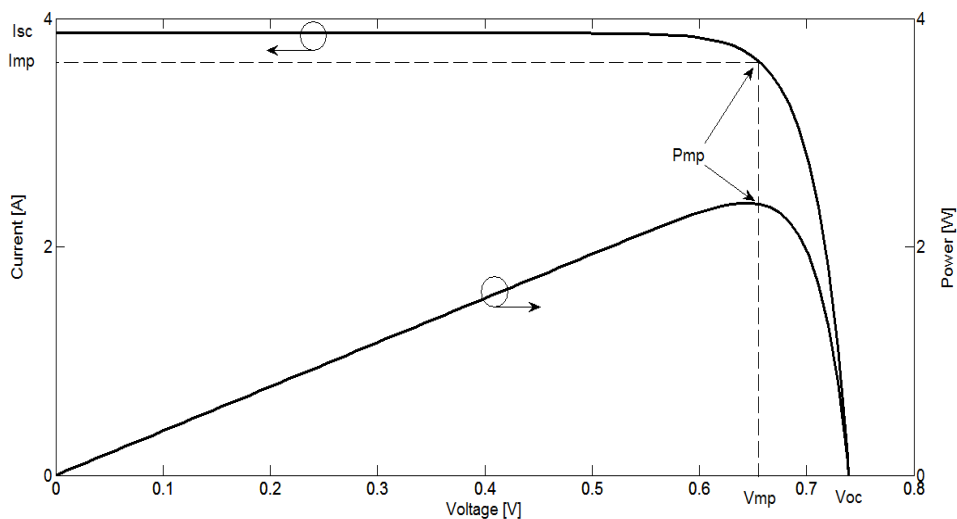


**Figure 2.1.4** – I-V and P-V curves representation, with the relevant current and voltage values.

Usually, these models fit experimental I-V characteristics accurately, and are often useful to obtain the model parameters. The parameters could be used to design the cell or module, and could be determined to optimize its performance. Also, “the model parameters can be a useful tool for monitoring cell manufacturing processes if the parameter values can be determined simply and rapidly” [16]. Due to the fact of being a first approach, we choose to work with the single diode model, considering the five parameters.

## 2.2 Determination of the characteristic current-voltage curve

Equation (4), in contrast to what happens with linear and quadratic algebraic functions, is a non-linear and transcendent equation that does not present an explicit analytical formula for its resolution, existing the need of finding numerical methods to solve it. A root finding algorithm is a numerical method or algorithm that allows finding a value  $x$  such that  $f(x) = 0$ , for a given function  $f$ . The  $x$  is called the root of that function [18]. In order to obtain the solution of the equation that describes the net current of the solar cell, one must take advantage of methods that deal with iterative processes. Those methods start by knowing approximated values of the root we want to find [18]. Examples of those methods are Bisection method, False Position method, Secant method, Newton method, *Müller* method [18].

The iterative process generates a succession of values,  $z_k$ , with associated errors, as

$$e_k = x - z_k \quad (6)$$

and because the iterative process should be a convergent process, it should be verified that:

$$\lim_{k \rightarrow \infty} z_k = x \quad (7)$$

The same is to say that

$$\lim_{k \rightarrow \infty} e_k = 0 \quad (8)$$

In [18] it is demonstrated how that error evolves with the number of iterations, and concluded that, in principle, if convergence rate is high, the number of iterations is small, depending on the required precision or tolerance. Although, this conclusion is not absolute and could lead to mistakes, because computational effort required must be considered. The main difference between local convergence methods and global convergence methods is that the firsts need to have initial values (starting values for the algorithms) as closer as possible of the solution we want to find, and the seconds do not [18].

## 2.2.1 Bisection method (Binary-Search or Bolzano)

Being  $f$  a continuous function in the finite interval  $S = [a, b]$ , and such that  $f(a)$  and  $f(b)$  have different signs, then function  $f$  have at least one zero (root) in that interval. Bisection method consists in constructing subintervals  $S_k = [a_k, b_k] \subset S = [a, b]$  by successive divisions in halves, for which also verifies that  $f(a_k)$  and  $f(b_k)$  have opposite signs [18]. In this way, a function root is being bound to successively smaller intervals. A schematic illustration was made for this numerical algorithm, presented in Figure 2.3.1.

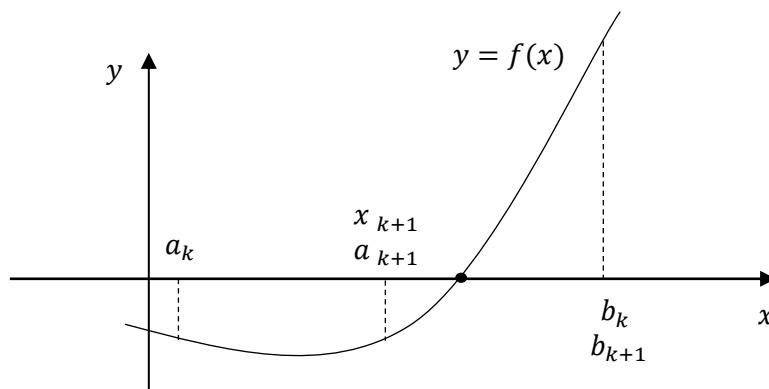


Figure 2.2.1 - Bisection method schematic illustration. Adapted from [18].

The algorithm flowchart of the Bisection method appliance is shown in Figure 2.3.2.

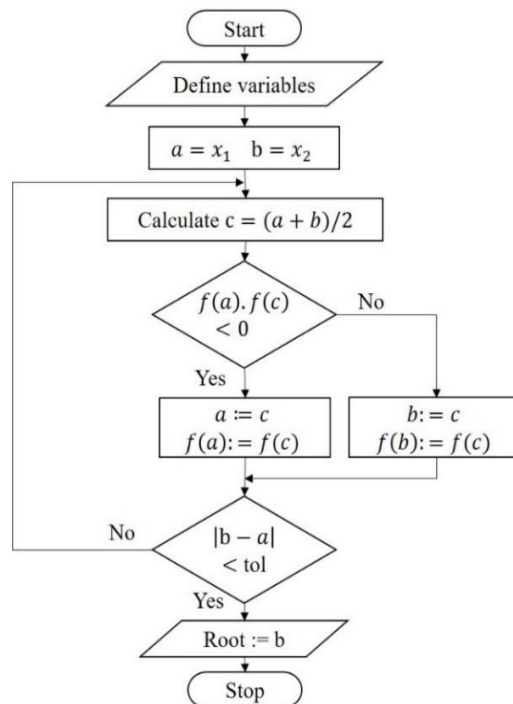
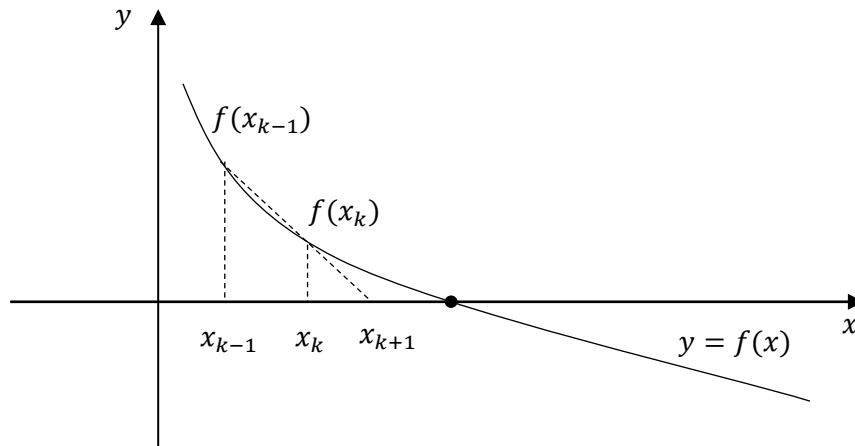


Figure 2.2.2 – Bisection method algorithm flowchart.

### 2.2.2 Secant method

Secant method consists of guessing two initial values,  $(x_{k-1}, f(x_{k-1}))$  and  $(x_k, f(x_k))$ , and obtain a next one,  $x_{k+1}$ , as the intersection of the secant defined by those points with the  $xx$  axis, as can be seen in the schematic illustration of this method presented in Figure 2.3.3.



**Figure 2.2.3** - Secant method schematic illustration. Adapted from [18].

The expression that allows obtaining the  $x_{k+1}$  value is

$$x_{k+1} = \frac{f(x_k)x_{k-1} - f(x_{k-1})x_k}{f(x_k) - f(x_{k-1})} \quad (10)$$

The algorithm flowchart of the Secant method appliance is presented in Figure 2.3.4.

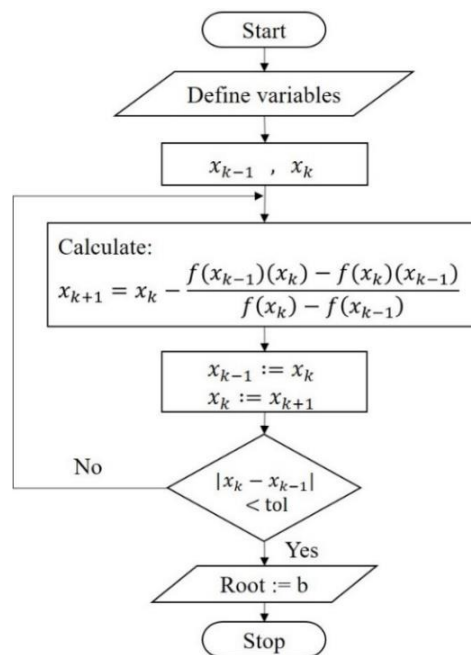


**Figure 2.2.4** - Secant method algorithm flowchart.

### 2.2.3 Newton-Raphson method

In the Newton-Raphson method, or simply Newton method, the curve is approximated with its tangent, as the schematic illustration of the method shows in Figure 2.3.5. The tangent intercepts the  $xx$  axis and this point is used as the new value of the approximation to the  $f$  root. The equation of the tangent to the function  $f$  at the point  $x_k$  is:

$$y = f(x_k) + f'(x_k)(x - x_k) \quad (11)$$

The intersection with the  $xx$  axis occurs in the value obtained from the following expression

$$x_{k+1} = x_k - \frac{f(x_k)}{f'(x_k)} \quad (12)$$

In this case, it is required to guess an initial value of  $x_0$ , which generate a succession  $\{x_k\}$  that will converge to the root of the function  $f$ . It is also required to compute its derivative,  $f'$ .

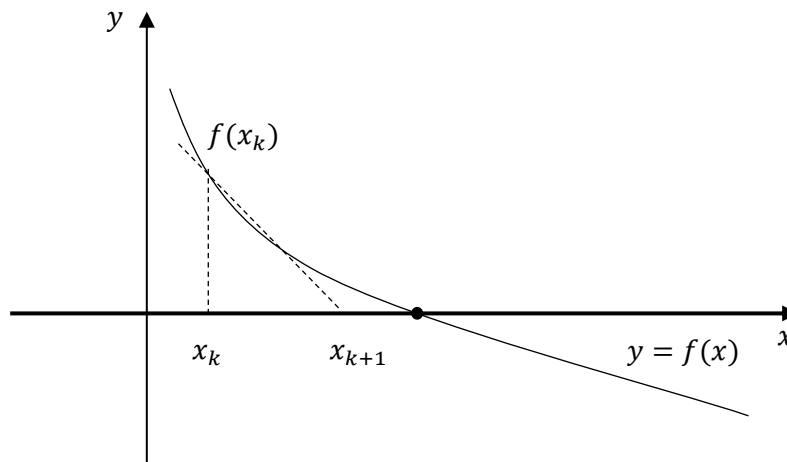


**Figure 2.2.5** - Newton-Raphson method schematic illustration. Adapted from [18].

The algorithm flowchart of the Newton-Raphson method appliance is presented in Figure 2.3.6.

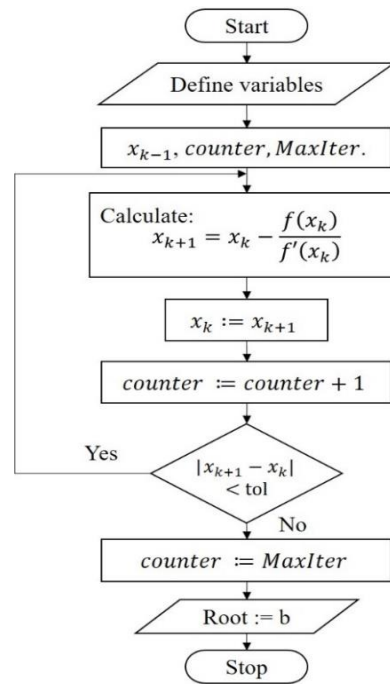


Figure 2.2.6 - Newton-Raphson algorithm flowchart.

### 2.3 Application results

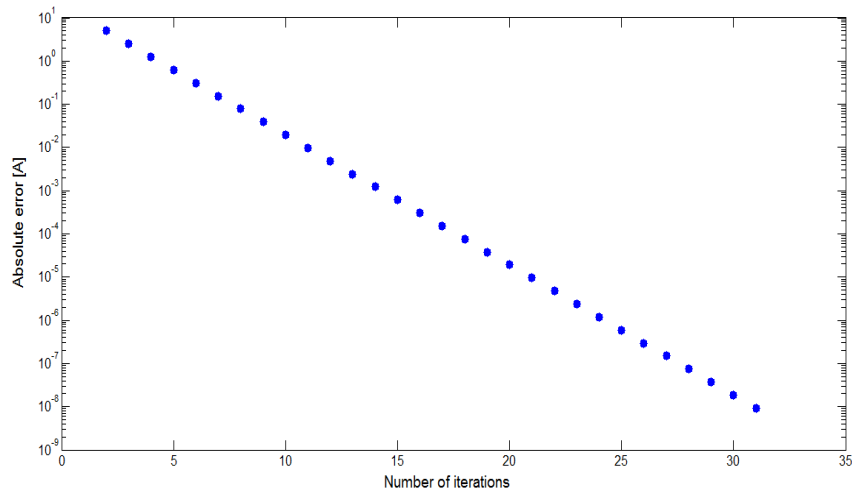
Bisection, Newton-Raphson and Secant methods were studied and applied in order to conclude which one of those algorithms is the best suited to make the description of the current-voltage curve. To apply the methods, ideal five parameters were used, described in Table 2.4.1, at a cells temperature of 25.00°C, which corresponds to 298.15K.

Table 2.3.1 - Parameters ideal values.

Parameter	$I_{ph}$ [A]	$I_s$ [A]	$n$	$R_{sh}$ [ $\Omega$ ]	$R_s$ [ $\Omega$ ]
Value	3.80	$1.00 \times 10^{-10}$	1.20	$1.00 \times 10^5$	$1.00 \times 10^{-5}$

#### 2.3.1 Bisection method

Bisection method was used to solve the current equation in the interval: [0.00-20.00] A, with an absolute error of  $10^{-8}$ , and in a voltage interval [0.00-0.76] V. The error is the difference between successive values of current between the iterations. The method takes several iterations until convergence is reached (namely thirty-one iterations, in this case), and the variation of the estimated error is presented in Figure 2.4.1, with all those iterations represented.



**Figure 2.3.1** - Error of Bisection method cycle, as a function of the number of iterations.

The stopping criterion is the absolute error of the calculated current, which is updated in each iteration step. In those conditions, thirty-one iterations were required. The result of this iteration procedure is the current in the circuit, for each given value of voltage.

### 2.3.1.1 Considerations

A rigorous convergence and error analysis of Bisection method is made in [18]. The Bisection method guarantee that convergence is always obtained in the defined interval for continuous functions, concluding that it is a global method. However, its convergence rate can be slow. This is the main reason why, generally, this method is used in a first phase of the works [18].

### 2.3.2 Secant method

To initiate the iteration procedure of the Secant method two initial values were required. Starting values of  $x_{k-1}$  of 3.70 A, and  $x_k$  of 3.80 A were used in this case. The absolute error of the current was  $10^{-8}$ , same as above. To verify if the method has the same response for all the voltage values used, the method was analysed independently for three distinct values: for the initial value of voltage range (0.00 V), a value in the middle of the voltage range (0.37 V), and a value near the end of the voltage range (0.73 V). The results are shown in the Table 2.4.2.

**Table 2.3.2** – Secant application results.

Voltage [V]	Iteration number	Current [A]
0.00	1	3.886924999611179
	2	3.886924999611179
0.37	1	3.886901373154788
	2	3.886901373154771
0.73	1	1.037954603564634
	2	1.037953465021237
	3	1.037953465020754

One can see in Table 2.4.2 that the function converges in two iterations in the beginning and middle of the interval of the voltage, and in the end of that interval the function converges in three iterations. In this way, one can conclude that the more far the solution is from the initial guessed values, a higher number of iterations are required.

### 2.3.2.1 Considerations

In this method, it is not required that the values of the function in subintervals extremes have different signs, which could mean that in some cases convergence is not absolute. The theoretical demonstration of Secant method convergence and error analysis is made in [18]. This method must be evaluated before use, in order to have the guarantee that the convergence is obtained with the function. Since Eq. (4) do not presented convergence problems, it was concluded that the method was well suited to use.

### 2.3.3 Newton Raphson method

Newton-Raphson method was applied to Equation (4), for the same conditions explained above. To start the iteration procedure of this method, an initial value of current,  $x_k$ , of 3.80 A was used. The function was applied to the same values of voltage presented before in 2.4.2, in the Secant method. The results of Newton-Raphson method are shown in Table 2.4.3.



**Table 2.3.3** - Newton-Raphson application results.

Voltage [V]	Iteration number	Current [A]
0.00	1	3.886924999611179
	2	3.886924999611179
0.37	1	3.886901373154779
	2	3.886901373154771
0.73	1	1.037954646347110
	2	1.037953465020761
	3	1.037953465020754

It can be seen that convergence is obtained in two iterations for the values in the lower end and middle of the voltage range, and in the upper end of that range three iterations are required. Newton-Raphson method convergence is fast with an initial value close to the solution.

#### 2.3.3.1 Considerations

The Newton-Raphson method, as in the case of the Secant method, may present convergence problems, and so a convergence and error analysis is explained in [18]. It is important to note that this method requires evaluating the derivative of the function, and so if the function is a very complex analytical expression, its derivative and computational programming become difficult, and so the choice of this method must be weighted. Because the convergence is quadratic, the Newton-Raphson method is one of the most used methods to non-linear equations [18]. In this case, using the Newton method with Eq. (4) did not showed any problem of convergence, and it is concluded that it is suitable method in this case.

## 2.4 Coupling Bisection and Newton-Raphson methods

Bisection method gives the guarantee of convergence; however, its slower convergence rate is a drawback. On the other hand, the Newton-Raphson method is the fastest one, due to its higher convergence rate (quadratic), which means that the accuracy is doubled in each one of the iterations [18]. Additionally, for some complex functions, the convergence of the method it is not guaranteed, which however it is not the case of Equation (4). Secant method is a fast method because it is a Newton-Raphson derivation, and it was interesting to analyse how to

ensure that derivative of the function offer no problem. Nevertheless, if initial value is not close to the root, there is no guarantee that the solution is reached, the same happening in the case of the Newton-Raphson method.

Taking into consideration the facts presented before, an idea to save a lot of computer processing, time and costs arise. The solution is to combine two of the methods presented before, namely the Bisection and Newton methods. The Bisection method should initiate the iteration procedure, and so one can assure that the method will converge. Because the function under study do not present problems in computing its derivative, Newton-Raphson method was chosen. The flowchart that describes the algorithm of the coupling of these two methods is shown in Figure 2.5.1.

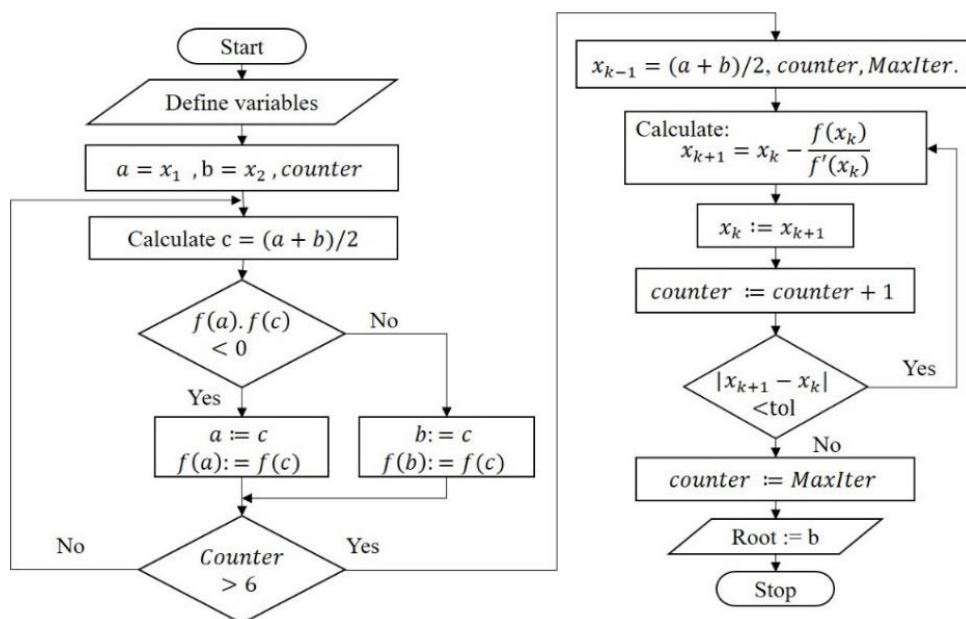


**Figure 2.4.1** – Flowchart for coupling Bisection and Newton Raphson methods.

### 2.4.1 Application results

For the coupled method, the same initial conditions as used before in Bisection method were also used. After a few iterations with Bisection method, the output value of current in that present iteration is taken and becomes the initial value of the Newton-Raphson method. In other words, from that iteration Bisection offers a good approximation of the solution to Newton-Raphson method, were this one starts and finish the iteration procedure.

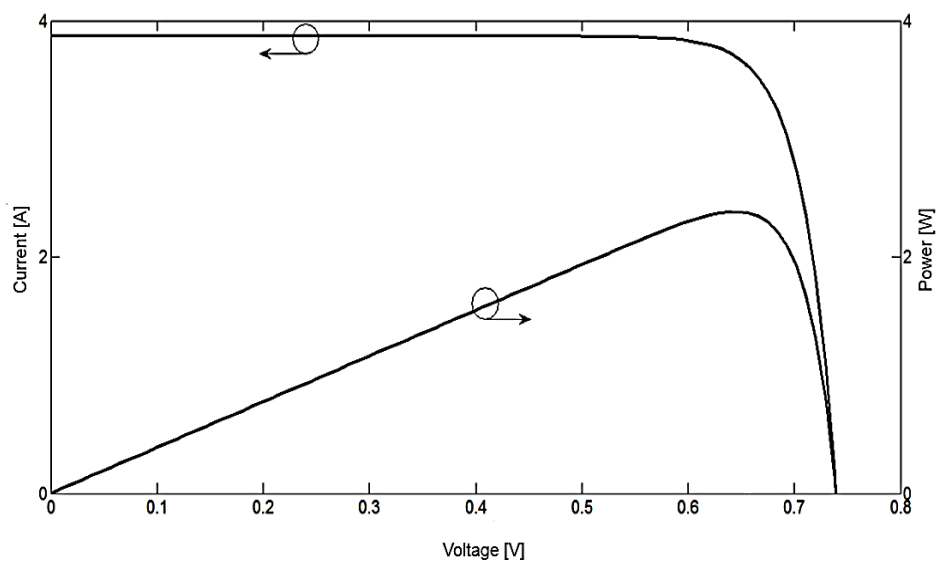
Table 2.5.1 shows the result of the iterative process, which starts with Bisection method and after the 6<sup>th</sup> iteration the algorithm changes to Newton-Raphson method that converges to the solution in two iterations.

**Table 2.4.1** – Results with coupled methods.

Voltage [V]		0.00	0.37	0.73
Method	Number of iterations	Current [A]		
Bisection	1	5.000000000000000	5.000000000000000	5.000000000000000
	2	2.500000000000000	2.500000000000000	2.500000000000000
	3	3.750000000000000	3.750000000000000	1.250000000000000
	4	4.375000000000000	4.375000000000000	0.625000000000000
	5	4.062500000000000	4.062500000000000	0.937500000000000
	6	3.906250000000000	3.906250000000000	1.093750000000000
Newton-Raphson	1	3.88692499961118	3.88690137315478	1.03795346509791
	2	3.88692499961118	3.88690137315477	1.03795346502076

This combined method allows a significant improvement of both methods in the way that convergence rate of Bisection method is not so slow and we have the insurance that Newton-Raphson method will converge to the solution because the initial guesses of the method are not so far from the solution. We can see that the function that describes the net current converges in a total of eight iterations starting from the same initial values as the pure Bisection method, which needed thirty-one iterations to converge. The photovoltaic cell output with this combined Bisection and Newton-Raphson methods is shown in Figure 2.5.2.

With those conditions, the maximum power output is 2.43 W.

**Figure 2.4.2** - Results of I-V and P-V curves of the coupling method.

# Chapter 3

## Parameters determination using the Nelder and Mead algorithm

The work presented in this chapter was developed aiming to describe and validate the Nelder and Mead algorithm applied to the determination of the five parameters of a photovoltaic module. The analysis is based in the values of the I-V characteristic curve, which are simulated based in the available data of a module. The response of the algorithm will be evaluated in three main paths, namely, the initial simplex maximum deviation, the imposed noise value of the current and the tolerance.

### 3.1 Determination of the parameters of a module

Previous section simulations were made using five ideal parameters. In this section, the five parameters which characterize the cell and module will be determined.

Parameters identification could be divided into three main categories, the analytical methods, which were investigated by many authors, as for example [16], the numerical methods, such as Newton-Raphson or Pattern Search, and the hybrid methods, such as cuckoo search hybridized with Nelder-Mead simplex (CS-NMS) [36]. These three main classes are summarized in Figure 3.1.1.

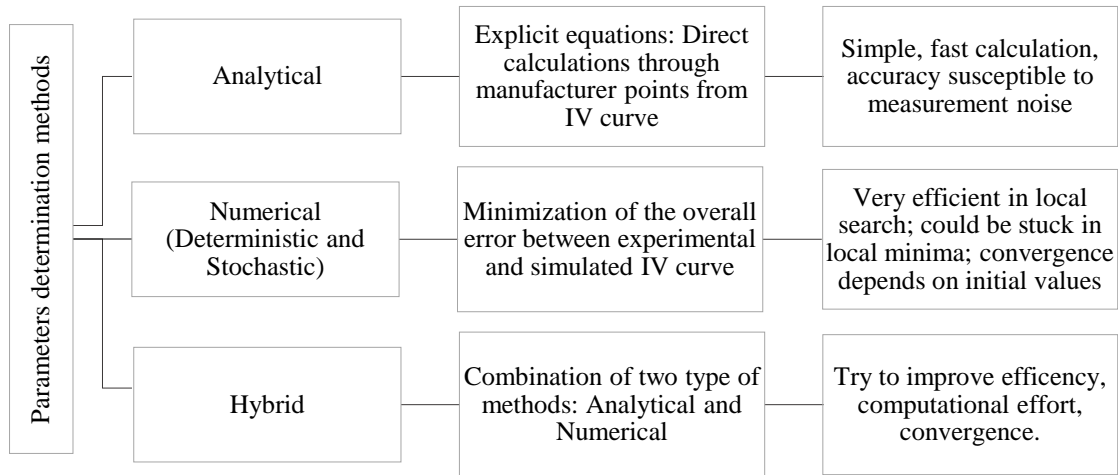


**Figure 3.1.1** – Methods to estimate the parameters. Adapted from [17].

We choose to work with a numerical algorithm, with the aim of observe its drawbacks and to evaluate its application feasibility to the solar photovoltaic.

### 3.1.1 The Nelder and Mead algorithm

Nelder and Mead algorithm is a simplex method, because its characterized by modifying the minimum or maximum search direction in each iteration. The first simplex concept known was presented by [23], which belongs to the direct search class. The simplex is a  $n + 1$  points set, that is a  $\mathbb{R}^n$  polyhedron with  $n + 1$  sides [21]. The simplex search consists of constructing a non-degenerate  $\mathbb{R}^n$  simplex, and simply using it to lead the minimum or maximum search [21]. In each iteration, the simplex methods choose the direction and amplitude based on its previous values of the parameters. For example, if a vertex is substituted by its reflection, i.e. a displacement of the vertex toward the opposite side, the result is also a simplex [21].

The Nelder and Mead optimization algorithm was firstly presented in 1965 by John Nelder and Roger Mead [20]. This method is usually applied to unconstrained minimization problems of a real-valued nonlinear function:  $f(x): \mathbb{R}^n \rightarrow \mathbb{R}$ , where  $n$  is the number of parameters to be optimized, and  $x = [x_1, x_2, \dots, x_n]^T$  the parameters vector [20]. The algorithm makes some movements, such as the expansion and contraction (toward inside the polyhedron) and shrinkage, in the better vertex direction. The simplex is a flexible geometric shape, and that is why the convergence prove is extremely difficult [21]. An illustration of the method is presented in Figure 3.1.2, a problem of two variables, where three vertices are required, being  $x_{worse}$  the vertex which one wants to reject, and  $x_{better}$  the vertex which one wants to keep:

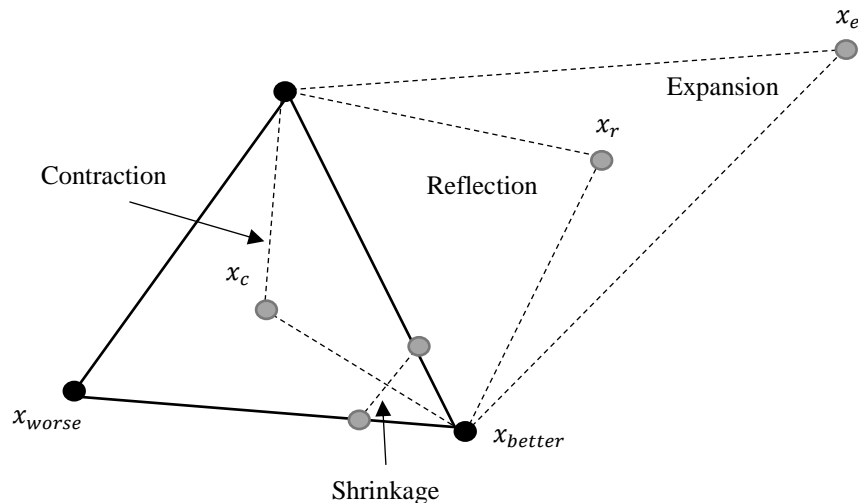


**Figure 3.1.2** - Nelder and Mead steps illustration, for a two variables problem.

For example, if the objective is to minimize the function and three vertices constitute the simplex, the function value is calculated in each of those vertices. The minimum value is the best vertex and the maximum value is the worst vertex. After those considerations, the simplex takes the worst vertex, and substitutes it by a contracted, reflected, expanded or shrunk vertex. The procedure continues until the minimum is reached.

### 3.1.1.1 General description

Considering an unconstrained optimization problem of  $n$  dimension, the following points shall be pointed out [21]:

- The method starts in a point through which one can start the search, which should be an initial approximation of the problem solution.
- The length between the vertices and the centre of the simplex, known as the barycentre or centroid, must be computed.
- Define an  $\mathbb{R}^n$  base, i.e. the basis of the vector  $e_i$ ,  $i = 1, \dots, n$  form the  $\mathbb{R}^n$  orthonormal base.
- The  $\alpha$ ,  $\gamma$  and  $\rho$  are the reflection, expansion and contraction coefficients. These coefficients values must verify the condition:  $0 < \rho < \alpha \leq 1, \gamma > 1$ . The shrinkage coefficient value is equal to 0.5.

The algorithm starts with the construction of a polyhedron in  $\mathbb{R}^n$ , with  $n + 1$  distinct vertices. After, the centroid of all points is calculated, and the values of the objective function

are determined for each vertice, and then sorted. Subsequently, and because our objective is the function minimization, the worst vertex,  $f_w$ , which is the highest value of the objective function, and the best vertex,  $f_b$ , which is the lowest vertex of the objective function are defined as [21]:

$$f_w = \max\{f_i\}, 1 \leq i \leq n + 1 \quad (13)$$

$$f_b = \min\{f_i\}, 1 \leq i \leq n + 1 \quad (14)$$

Then, the worst vertex is substituted with a new vertex, and thus a new simplex, with  $n$  vertices, is obtained. The acceptance or rejection of the new points is based on the comparison of the values of the objective function, and are based on the centroid of the  $n$  best vertices [21].

Being the simplex  $\{x_i\}_{i=1}^{n+1}$  in  $\mathbb{R}^n$  and the worst vertex the one with index  $p \in \{1, 2, \dots, n + 1\}$ , the centroid of  $n$  best vertices of the simplex is given by:

$$x_0 = \frac{1}{n} \sum_{\substack{i=1 \\ i \neq p}}^{n+1} x_i \quad (15)$$

Whatever the final simplex is, the values of the objective function,  $f$ , are calculated, and the identification of the vertices is made again, in order to initiate the next iteration. The algorithm ends when the convergence is obtained [21], according to the convergence criterion.

Nelder and Mead algorithm simplex is widely accepted, being considered the most used simplex algorithm of all direct search methods, in numerical optimization software packages. The original algorithm was published in [20], which is a classical scientific citation, with numerous references in scientific journals, and that is one of the main reasons to the existence of several variants of this method [21].

The auxiliary steps of the algorithm, including the selection of the new vertex in each iteration step, are described in the Table 3.1.1. The flowchart of the algorithm is shown in Figure 3.1.3.

**Table 3.1.1** - Steps of the Nelder and Mead algorithm [20].

Steps	Operation	Description
1	Initial simplex	Construction of the initial simplex, with $n + 1$ vertices: $x_1, x_2, \dots, x_{n+1}$ , in the $n$ -dimensional space.
2	Order	Order of the vertices by calculation of the values of the function which one want to minimize, i.e.: $f(x_1) \leq f(x_2) \leq \dots \leq f(x_{n+1})$ . The best vertex is $x_1$ and the worst vertex is $x_{n+1}$ .
3	Centroid	Calculation of the centroid of all vertices, $x_0$ , except the $x_{n+1}$ vertex.
4	Reflection	Calculation of the reflected vertex, $x_r = (1 + \alpha)x_0 - \alpha x_{n+1}$ , where $\alpha$ is a positive constant, the reflection coefficient. If the reflected vertex is better than the second worst, but not better than the best, i.e., $f(x_1) \leq f(x_r) < f(x_n)$ , obtain a new simplex, by replacing the worst vertex by the reflected vertex, $x_r$ , and return to step 1.
5	Expansion	If the reflected vertex is the best vertex so far, i.e., $f(x_r) \leq f(x_1)$ , calculation of the expanded vertex, $x_E = \gamma x_r + (1 - \gamma)x_0$ , where $\gamma$ is the expansion coefficient, which is greater than the unity. If the expanded vertex is better than the reflected vertex: $f(x_E) \leq f(x_r)$ , obtain a new simplex, replacing the worst vertex, $x_{n+1}$ , with the expanded vertex, and return to step 1. Else, obtain a new simplex, replacing the worst vertex by the reflected vertex, and return to step 1.
6	Contraction	If one gets here, it is certain that $f(x_r) \geq f(x_n)$ . Computation of the contracted vertex, $x_c = \rho x_r + (1 - \rho)x_0$ , where $\rho$ is the contraction coefficient, which lies between 0 and 1. If the contracted vertex is better than the worst vertex, i.e., $f(x_c) < f(x_{n+1})$ , obtain a new simplex by replacing the worst vertex by the contracted point $x_c$ and return to step 1.
7	Shrinkage	Replace all vertices, except the best, by $x_i = x_1 + \sigma(x_i - x_1)$ .



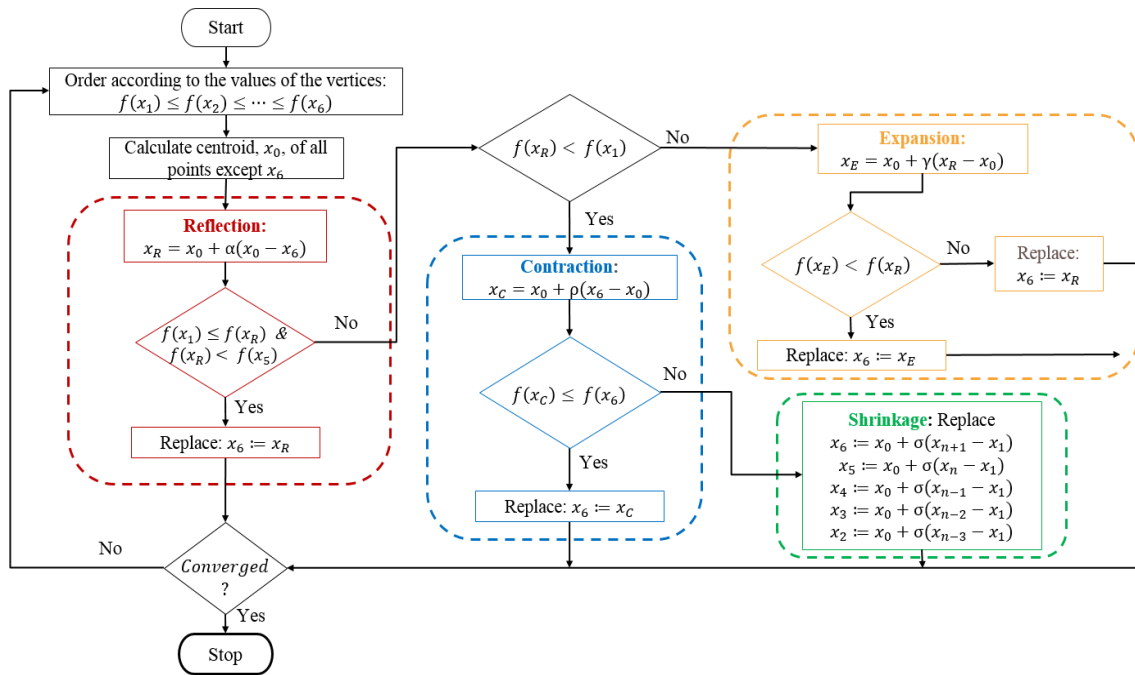


Figure 3.1.3 - Flowchart of the Nelder and Mead algorithm.

Legend of Figure 3.1.3:

$x_0$  – Centroid of all vertices, except the worst vertex;  $f(x_n)$  – Value of the function calculated in the  $n$  value;  $\alpha$  – Reflection coefficient;  $\gamma$  – Expansion coefficient;  $\rho$  – Contraction coefficient;  $\sigma$  - Shrinkage coefficient.

Simplex vertex where function gets:

- $x_1$  – the smallest value.
- $x_2$  – a higher value than the one calculated with  $x_1$ .
- $x_3$  – a higher value than the one calculated with  $x_2$ .
- $x_4$  – a higher value than the one calculated with  $x_3$ .
- $x_5$  – a higher value than the one calculated with  $x_4$ .
- $x_6$  – the higher value.
- $x_R$  – the reflected value.
- $x_E$  – the expanded value.
- $x_C$  – the contracted value.

### 3.1.1.2 Stopping criterion

Since the initial work of Nelder and Mead, several authors made modifications in the method, improving the convergence to the respective problem [21]. Some of those authors proved the method's limitations in its overall convergence [21]. The convergence properties are only demonstrated for lower dimensions, of one dimension convex functions. In [21] the results showed the algorithms robustness in  $\mathbb{R}$ . None of the proven properties guarantees the method convergence in high dimensions. On the other hand, there are several approaches to the vertices acceptance. In conclusion, the method may fail because of insufficient assurance of descent to a minimum of the objective function, or even converge to a non-stationary point, which deteriorates the simplex geometry [21].

The used stopping criterion is based on the least squares method, in which the objective function is the difference between the measured and the simulated values, expressed as:

$$S_f = \frac{1}{N} \sqrt{\sum_{i=1}^N (I_{(\widehat{p})i} - I_{(p)i})^2} \quad (16)$$

where,

$I_{(\widehat{p})i}$  – Estimated current value [A];

$I_{(p)i}$  – Experimental current value [A].

The objective is to minimize this function. The choice was an intensive challenge, since the centroid could be put to vary, however the uniformity of the simplex could deteriorate, or worse, it could easily be maintained in two consecutive iterations, with the cost function value far from the minimum value. The obtained values in two consecutive iterations should be compared, and could present an insignificant difference, but the centroid can easily change.

These and other questions led to successive attempts, drawing to the conclusion that the choice should be made in the way of considering the centroid and vertices of the simplex together. One stopping criteria that proved to be the tighter criterion experienced is presented next. The cycle stops when the maximum value of the distances from the vertices of the simplex to the centre of the simplex (or barycentre) is smaller than the imposed tolerance of the cycle. Figure 3.1.4 presents the stopping criterion, with a three vertices example. The maximum absolute value of these distances is the comparable value with the tolerance of the cycle.

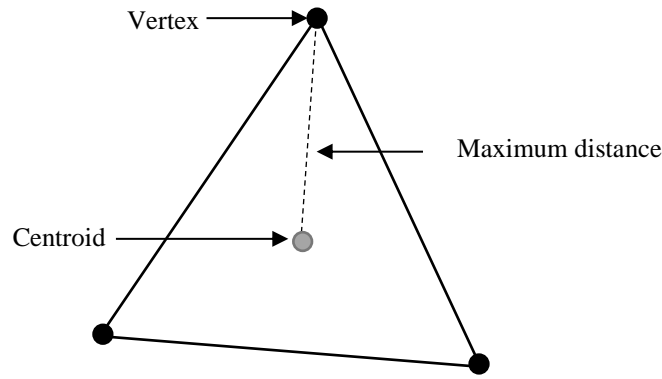


**Figure 3.1.4** - Stopping criterion illustration, with a three vertices example.

Thus, it is necessary to calculate the value of the centroid in each iteration, to, subsequently, calculate the distance from the vertices of the simplex to the centroid, and finally to seek for the maximum absolute value of these distances, which is the comparable value with the guessed tolerance (the absolute maximum distance higher than the cycle tolerance).

### 3.2 Determination of guess values of the parameters for the initial simplex

If not well chosen, the parameters that describes the photovoltaic characteristic curve of the cell can move its operation away from the maximum power point. To contour this problem, in an ideal photovoltaic cell, there are standard values for which the photovoltaic cell shows ideal response [25]. These parameters have direct impact on the power output and can be divided in internal (physical) and external (environmental) parameters. Those ideal values don't hold in real time operation, due to the change of the external parameters.

A sensitivity analysis of the parameters of the single diode model should be made, because the guessed vertices which initiate the Nelder and Mead algorithm are dependent of the initial conditions choice [21]. This choice is the estimation of the parameters from upward or from below. The research group worked in this matter, in [25] and [26]. The works allow a fastest convergence to the solution of the Nelder and Mead algorithm, i.e helps the algorithm to not get stuck that easily in an untrue solution.

In [25] and [26] an evaluation of the impact of internal and external parameters variation was carried out starting from its standard values and using the error function presented in Equation (17). White noise was added to produce real-time data of output simulation values.

$$E(I) = \frac{1}{N} \sqrt{\sum_{i=1}^N (I_{std} - I_{err})^2} \quad (17)$$

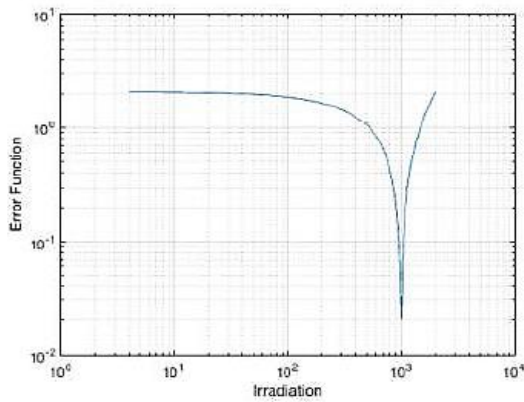


**Figure 3.2.1** - Error function vs. Irradiance [W/m<sup>2</sup>] [26].

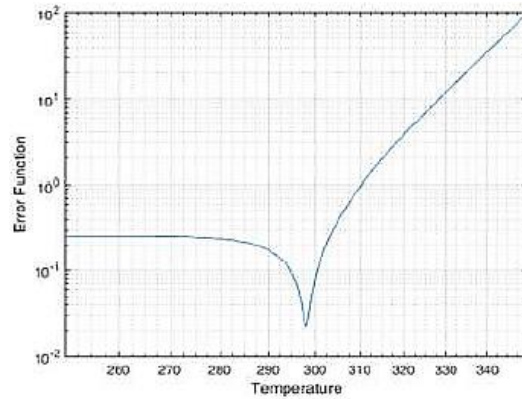


**Figure 3.2.2** - Error function vs. Cell temperature [K] [26].

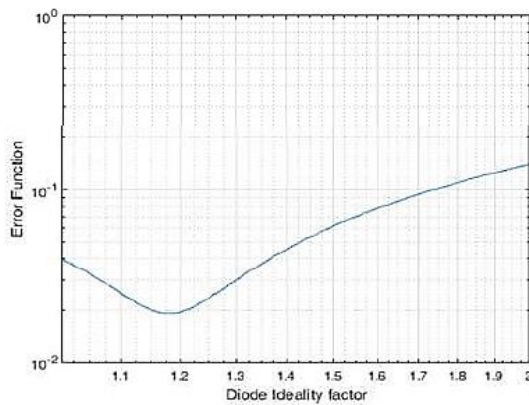


**Figure 3.2.3** - Error function vs. diode ideality factor [26].

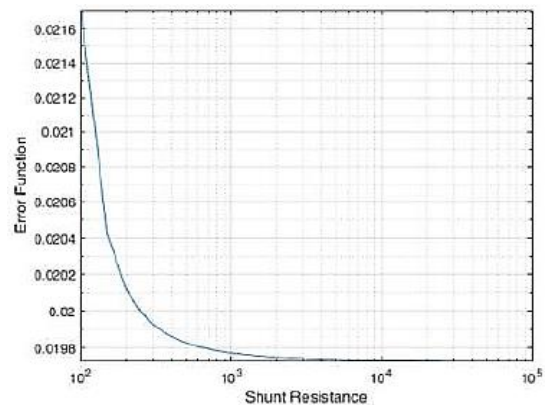


**Figure 3.2.4** – Error function vs. shunt resistance [Ω] [26].

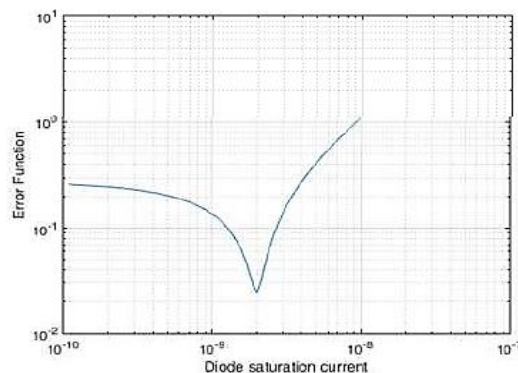


**Figure 3.2.5** - Error function vs. diode saturation current [A] [26].

In [25] and [26] five parameters were analysed: the irradiance, cell temperature, diode ideality factor, shunt resistance and diode saturation current. As it can be seen in Figure 3.2.1, irradiance should be estimated slightly upward its standard value. The cell temperature, presented in Figure 3.2.2, should be estimated also upward. The ideality factor, Figure 3.2.3,

should be estimated upward. In Figure 3.2.4 the shunt resistance is presented, indicating that should be estimated from below. The Figure 3.2.5 shows the diode saturation current, which should be estimated from upward.

Regarding the series resistance, in [26] it is verified that the obtained curve is nearly constant, evidencing any response. This shows that this resistance has low effect in the output of the solar cell [25]. The value of the series resistance is normally very small and near to zero [25]. For small variation among the values of series resistance, it does not show any abrupt change, demonstrating that is not a sensitive parameter comparing to the other parameters [26].

### 3.3 Application of the Nelder and Mead for the five parameters model based on the available data of a module

The Nelder and Mead algorithm evaluation is firstly made by simulating the current and voltage values from an existing module of the market, based on its datasheet values.

The obtained results will be divided into three crucial aspects, namely, the dependence that the algorithm presents regarding the values that constitute the initial simplex, the effect of the imposed tolerance and, finally, the qualification of noise response, in order to better understand how the method convergence is affected, according to the difference between the simulated and obtained current values. In the following, the main results are presented.

The selected module is the Sunrise Solartech, model SR-M654225, and the manufacturers data most relevant features, measured under STC conditions, were consulted in [37] and are shown in Table 3.3.1.

**Table 3.3.1** – Characteristics of the module Sunrise Solartech SR-M654225 [37].

Characteristic	Value
Cell material, cell number	Monocrystalline Silicon, 54
Module area [ $m^2$ ]	1.47
Nominal efficiency [%]	15.32
Maximum power [W]	225.07
Voltage at MPP [V]	27.10
Current at MPP [A]	8.30
Open circuit voltage [V]	33.40
Short circuit current [A]	8.90

The other parameters of this module were obtained from the NREL System Advisor Model (SAM) library editor, in the CEC (California Energy Commission) performance model section [37]. The University of Wisconsin-Madison Solar Energy Laboratory's have a five parameters model with a database of module's parameters. These parameters are calculated through standard reference condition data provided by the manufacturer of the module or by independent testing laboratory [37].

Having those parameters, the Newton-Raphson was used, aiming to achieve the current and voltage values. The choice of using the Newton-Raphson method is due to the fact of this method did not present obstacles of derivative and initial guesses, and because it has the fastest convergence of the studied methods in Chapter 2. The Nelder and Mead coefficients used in this work are the standard values, and are presented in Table 3.3.2.

**Table 3.3.2** - Standard coefficients of the Nelder and Mead algorithm [20].

<b>Nelder and Mead coefficient</b>	<b>Symbol</b>	<b>Value</b>
Reflection	$\alpha$	1
Expansion	$\gamma$	2
Contraction	$\rho$	0.5
Shrinkage	$\sigma$	0.5

The main objective of this topic is to compare the obtained results with the parameters obtained from the SAM software in STC conditions and make some variations on the imposed current noise, tolerance and initial simplex, to evaluate the algorithm response. These parameters are presented in Table 3.3.3.

**Table 3.3.3** – Reference parameters for the Sunrise Solartech SR-M654225 module [37].

Parameter	$I_{ph}$ [A]	$I_s$ [A]	$n$	$R_{sh}$ [ $\Omega$ ]	$R_s$ [ $\Omega$ ]
NREL value	8.961	$4.310 \times 10^{-9}$	1.200	168.950	0.216

### 3.3.1 Initial simplex numerical tolerance

Assuming that the parameters of Table 3.3.3 describe the characteristic curve of the considered module, the response of the algorithm was evaluated, considering the choice of the initial vertices, which compose the simplex. The chosen tolerance was  $10^{-12}$ .

In this case, the presented parameters were used to simulate the curve at STC conditions, over which is applied noise, in order to analyse the discrepancies between the results obtained by the simulated and the estimated values. Therefore, the dependence on the simplex initial values is analysed, with a fixed current imposed noise of 30% of the rms. Thus, maximum deviations of 10%, 30%, 50%, 70% and 90% from the initial curve were simulated, as can be observed in Appendix 2. Figure 3.3.1 presents the relative difference between the parameters of NREL and the obtained values using the Nelder and Mead algorithm, as a function of the initial simplex maximum deviation, in percentage.

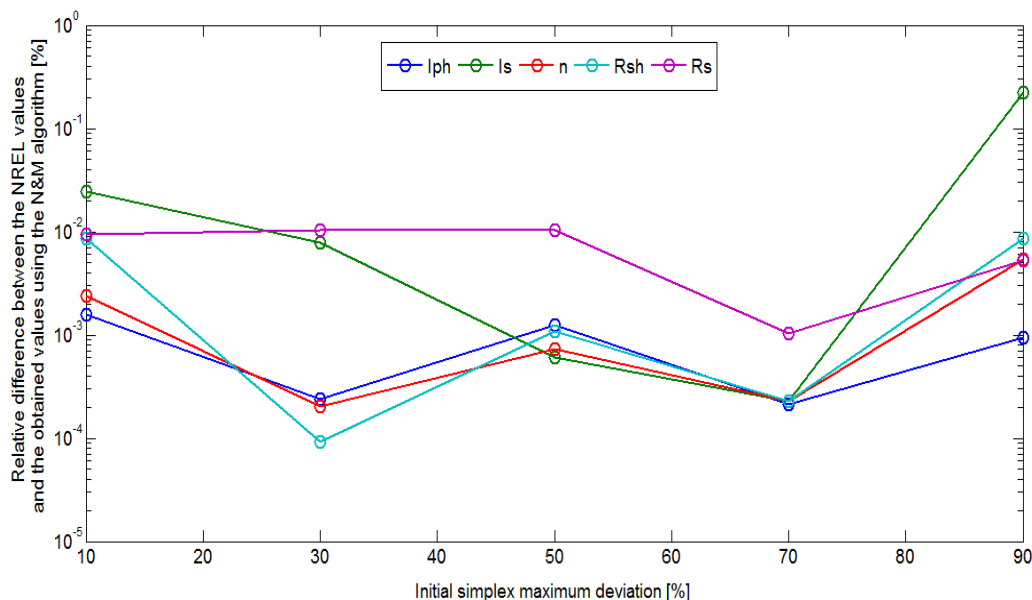


**Figure 3.3.1** – Relative difference between the obtained values with the Nelder and Mead algorithm and NREL values as a function of the initial simplex maximum deviation.

From Figure 3.3.1, it is possible to conclude that the algorithm converges to a value lower than 1% of the relative difference between the NREL values and the estimated ones, for values lower than or equal to 90% of the initial simplex, for all the five studied parameters. In this way, the algorithm ensure a very good photovoltaic characterization either with an initial simplex maximum deviation close or far from the convergence solution.

These results were obtained after several attempts on the guessed values of the initial simplex, only achieved through the performed sensibility analysis of the parameters and stopping criterion of the cycle. The Nelder and Mead algorithm convergence depends on the guessed initial simplex (guessed initial vertices, which will compose the polyhedron).

### 3.3.2 Imposed noise from the initial curve

The noise imposed from the initial curve is here analysed. The chosen tolerance was  $10^{-12}$ , as before, and the initial simplex maximum deviation a value of 30% was used. It was analysed the values of noise from 5% to 90%, which can be observed in Appendix 1.

The Figure 3.3.3 shows the effect of the imposed noise, comparing the difference between the NREL values and the obtained values of the parameters using the Nelder and Mead algorithm.

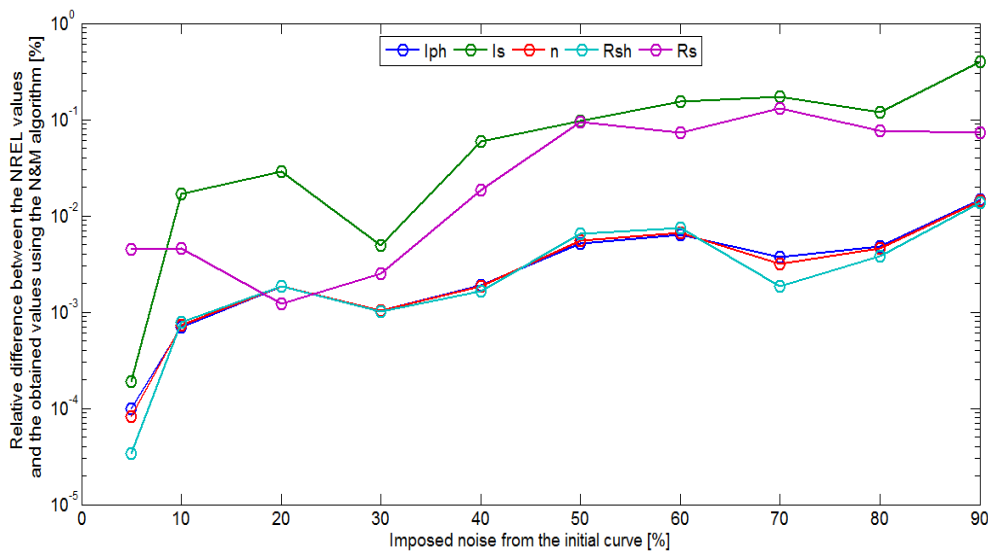


**Figure 3.3.2** - Difference between Nelder and Mead results and NREL values, as a function of the noise in the current measurements.

From Figure 3.3.3, one can observe the impact that this variable has on the determination of the parameters. The relative difference between the values of Table 3.3.3 and the estimated values are lower than 1%, offering a good characterization, with the constant values of tolerance and of initial simplex maximum deviation.



It can be seen that with the rising of the imposed noise, the relative difference increases, so it can be concluded that the quantity of noise is important for a good photovoltaic characterization.

### 3.3.3 Cycle tolerance and stopping criterion

In order to evaluate the tolerance impact (which is directly related with the stopping criterion) on the parameters determination, the current noise used was of 30% from the root mean square original curve, and with a maximum deviation of the initial simplex of 30% from the assumed real values of Table 3.3.3. The data was collected and organized in Figure 3.3.4.

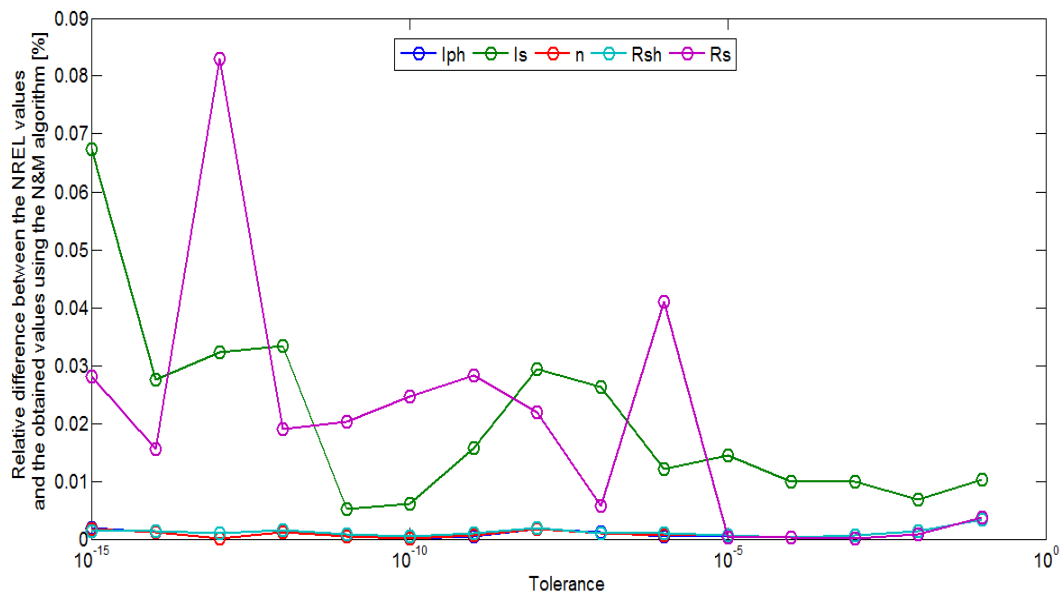


**Figure 3.3.3** - Difference between Nelder and Mead results and NREL values, as a function of the tolerance.

From Figure 3.3.4 it can be concluded that the analysed values of tolerance offers an insignificant impact – smaller than 0.1% - on the parameters achievement, in the analysed conditions. With a tolerance decrease, one should expect the decrease of the relative difference between the obtained parameters and the assumed real parameters, which does not happen with uniformity. Although the relative difference is still very low in the biggest differences (near 0.07% or 0.08% values), one could observe uniformity in the photo-generated current, ideality factor and shunt resistance values, but not with the series resistance and reverse saturation current values. What is happening is that with a very minimum

tolerance, the convergence of these values starts to become limited, and beyond the tolerance of  $10^{-15}$  of the Nelder and Mead algorithm the convergence is not obtained.

This analysis showed that with a minimum tolerance does not always offer the best convergence results. The time response of the algorithm was not accounted in this study, although with a decrease in the tolerance the convergence is slower.

### 3.4 Considerations

Nelder and Mead algorithm was computed and tested to obtain the parameters of a photovoltaic module, based in the single-diode model, considering the five parameters. Following those considerations, the Nelder and Mead method proved to be a robust method for the parameters estimation. The study showed that the convergence of the algorithm is dependent on the guessed initial simplex constitution, because if the input values of the vertices of the simplex are from an order of magnitude very different from the real parameters, the algorithm may not converge, and the sensitive analysis made in [25, 26] proved to be a crucial step. Another consideration is that the existence of local minimums or maximums may exist, which can obstruct the Nelder and Mead convergence to the solution.

# Chapter 4

## Nelder and Mead algorithm development and experimental validation

Current chapter has the aim of applying the Nelder and Mead algorithm based in the current and voltage measurements from a module, obtained through a laboratorial experiment, which will be briefly described. The algorithm will be integrated with a thermal model of the module, to estimate the temperature of the cell, five parameters and maximum power output.

### 4.1 Materials and methods

The instrumentation needed to fulfil the laboratorial experiment comprises a photovoltaic module, a data acquisition board, a function generator, a GPIB device, a load resistance, a sensor of wind speed and air temperature, a sensor of the module backsheet and glass surfaces, an artificial source of irradiation and a computer to storage the data. The configuration schematic of the experimental setup is shown in Figure 4.1.1.

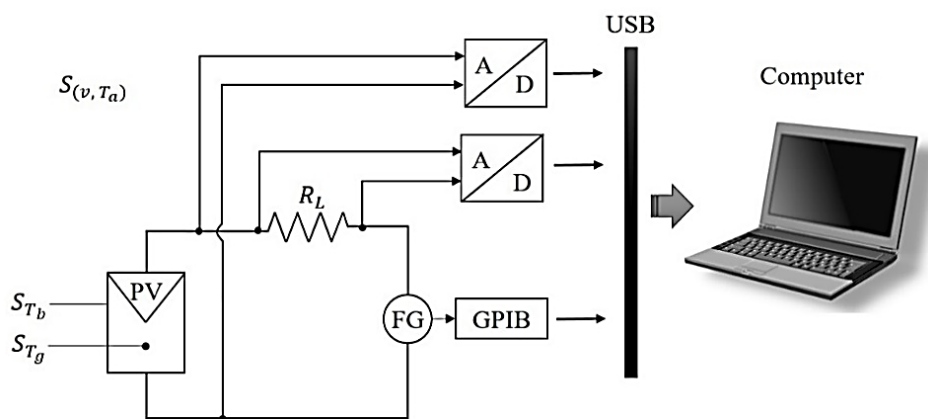


**Figure 4.1.1** – Schematic of the laboratorial experiment.

Legend of Figure 4.1.1:

A/D – Data acquisition board (analog to digital converter).

FG – Function generator.

GPIB – Function generator controller.

$R_L$  – Load.

PV – Photovoltaic module.

$S_{(v,T_a)}$  – Wind speed and air temperature sensor.

$S_{T_b}$  – Backsheet surface temperature sensor (probe).

$S_{T_g}$  – Glass surface temperature sensor (probe).

USB – Universal Serial Bus cable that makes the connection between the instruments and the computer.

#### 4.1.1 Data acquisition system

A data acquisition board allowed measuring the surrounding environment conditions. Most of the surrounded information has analogical nature and the data acquisition task is to convert the sensors analogical signals into digital signals [38]. Data acquisition consists of measuring electrical or physical phenomena, as voltage, current, temperature, pressure, or sound. Each data acquisition system is defined by the requirements of the application, having in common the purposes of acquire, analyse and report information. Data acquisition systems incorporate signals, sensors, actuators, signal conditioning, data acquisition devices and application software [39].

In this experiment, it was used the NI USB-6009 board, which is a data acquisition device from National Instruments. The device provides eight single-ended analog input channels, two analog output channels and 12 digital Input/Output channels. The NI-DAQmx driver software should be installed to read the data through MATLAB software [39]. The characteristics of this instrument could be consulted in the datasheet of the instrument, resumed in Appendix 3 [39].

### 4.1.2 Function Generator and GPIB devices

A function generator is an electronic device that is usually used to generate electrical waveforms, with different frequencies. The most common waveforms produced by the function generator are the sine, square and triangular functions. The function generator is applied in this experiment as a signal source, with the aim of testing the solar photovoltaic module signal output (current and voltage). The function generator used in this experiment is the Arbitrary Function Generator SONY Tektronix, model AFG320 [40]. The details of this instrument are presented in Appendix 4 [40].

Because the function generator is manually controlled, a General-Purpose Interface of Bus (GPIB) device is used to control automatically the waveform output of the function generator, according the received data. GPIB returns the signal with adequate frequency, offset and amplitude. The device used is the GPIB-USB-HS [41]. GPIB is a standard interface in industry to electronic measurements test. The GPIB is the interface between the computer and the instruments. The computer, in this case, controls it by MATLAB code, and it sends the information to the instrument that needs to be configured, performing its automatic correction. The main characteristics of this device are presented in Appendix 4 [41].

### 4.1.3 Photovoltaic module and artificial source

The values that characterize the module are presented in Table 4.1.1 and are the mean values measured from experimental I-V curves.

**Table 4.1.1** – Main measured characteristics of the photovoltaic module.

Characteristic	Measured value
Area [ $m^2$ ]	$3.68 \times 10^{-2}$
Number of cells	14
Maximum power [W]	$7.13 \times 10^{-1}$
Voltage at MPP [V]	6.05
Current at MPP [A]	$1.18 \times 10^{-1}$
Open circuit voltage [V]	9.01
Short circuit current [A]	$1.52 \times 10^{-1}$

The artificial source is a 1000W halogen lamp, with 2900K color temperature [42]. A pyranometer was used to quantify the incident radiation that the surface of the module receives. Its calibration constant is  $11.19 \mu V/m^2$ . The measured voltage on the pyranometer was  $3.12 mV$ , and in this way, the module received an irradiation of about  $278 W/m^2$ . The distance between the module and the source was about  $1.05 m$ . The obtained values do not match the STC or NOTC conditions.

#### 4.1.4 Instrumentation for air temperature and wind speed measurement

To determine the room temperature and air speed, a weather sensor was needed to install in the place. To this end, an integrated weather sensor of the Institute of Earth and Sciences was installed, namely a Vaisala Weather Transmitter, model WXT536. This instrument allows data collection of environmental variables such as wind speed and direction, air humidity, air temperature, atmospheric pressure, precipitation. The instrument is connected to a computer through an USB port, which has dedicated software that allows recording in real-time the measurement data. In this case, we only were interested in the ambient air temperature and air speed in the room. The main specifications of this instrument are presented in Appendix 5, based in its datasheet [43].

#### 4.1.5 Temperature sensor with digital display

To measure the temperature of the solar module, a digital display thermometer was used, to obtain both the temperature of the glass cover and of the “backsheet”. The characteristics of the digital display are presented in Appendix 6 [44].

The sensing elements (temperature probes) were placed in contact with the areas whose temperature is to be measured and then connected to the digital display. In this case, two separate probes were used, for the glass cover and backsheet, respectively. Additionally, the digital display thermometer was connected to the data acquisition board, in the way that these measurements were also recorded in the computer. The main characteristics of this instrument are presented also in Appendix 6 [45].

## 4.2 Integrated algorithm for determination of cell temperature, model parameters and maximum power output

With the help of the data acquisition board, the voltage and current data were measured and the I-V curve obtained. Nelder and Mead algorithm is then applied to determine the correspondent model parameters by fitting the characteristic curve to measured data. A very important aspect in the parameter estimation is the determination of the cell temperature in operation conditions other than the standard test conditions under a controlled environment. In this way, the cell temperature was estimated and included in the cycle, thus allowing the final parameters calculation even for tests under real operation conditions.

The flowchart of this algorithm for determination of cell temperature, model parameters and power output at MPP, under the given environmental conditions of irradiance, air temperature and wind speed, is shown in Figure 4.2.1.

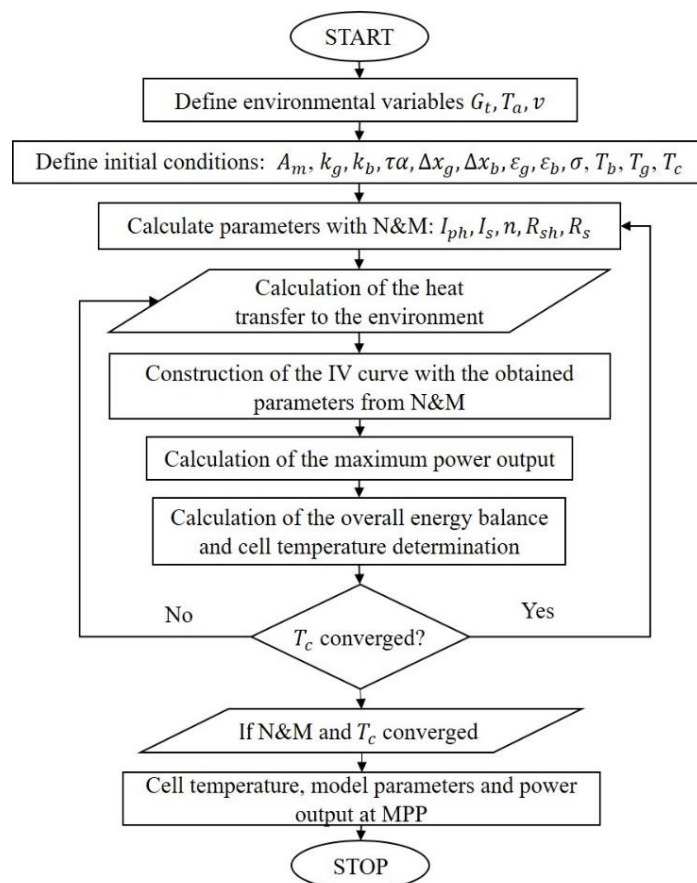


**Figure 4.2.1** – Flowchart of the algorithm for the determination of cell temperature, model parameters and power output at MPP.

### 4.2.1 Estimation of cell temperature based on measurements

To estimate the temperature value at which the cells were at the experiment, the values of the function of the least squares method which results of the Nelder and Mead algorithm application were collected and traced with the temperature variation. Thereby, it's possible to verify the value of this function for which the temperature is minimum, shown in Figure 4.2.2.

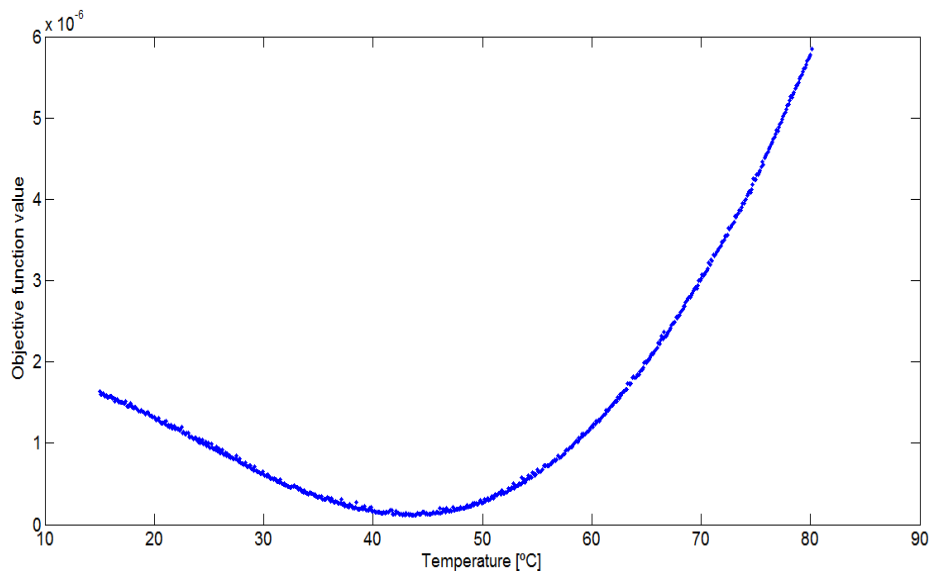


**Figure 4.2.2** - Cost function as a function of the variation of the cell temperature.

Through a fourth polynomial fitting, it's possible to conclude that the temperature value for which the function value is minimum is 43.44°C, which corresponds to 316.59K.

### 4.2.2 Thermal model of the photovoltaic module and cell temperature determination

Solar irradiance and cell temperature are variables that directly affects the photovoltaic cell operation and power output. Cell temperature is a sensitive parameter of the photovoltaic cell, as the efficiency strongly depends on its temperature. This temperature can be calculated through a global energy balance of the cell and by knowing the fraction of energy that is absorbed by the cell and converted into sensible heat (thermal energy). Generally, increasing temperature means lower performance, which means that losses are higher because more absorbed energy is converted to heat and not in electricity [7].

The increase of the cell's temperature has as result the decreasing of the power output, with the correspondent decrease of the open circuit and reverse saturation current. A cell



temperature increase may indicate poor ventilation, induced by wind [4]. The exact cell temperature is difficult to measure experimentally, and this is the main reason of its estimation. Present method is based on an iterative process, in which the ambient temperature, solar irradiance and wind speed are the imposed external environmental conditions.

Heat transfer to the environment is estimated, through an energy balance to the photovoltaic module. This thermal analysis requires the heat transfer coefficients calculation, thus enabling the global heat losses estimation, and the useful power obtained in the photovoltaic conversion as a function of the incident irradiance. Figure 4.2.3 illustrates the photovoltaic module energy balance model made.

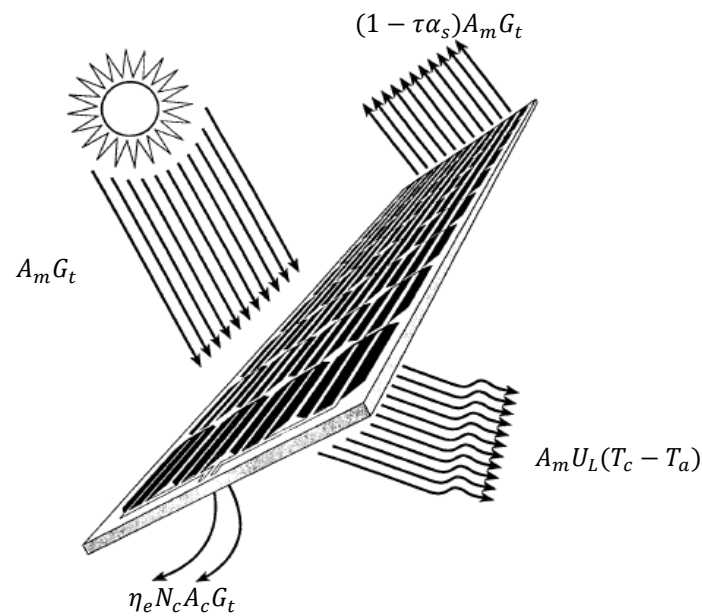


**Figure 4.2.3** - Energy balance of a solar photovoltaic module. Adapted from [46].

Legend of Figure 4.2.3:

$A_m$  – Area of the photovoltaic module [ $m^2$ ].

$A_c$  – Area of each photovoltaic cell [ $m^2$ ].

$G_t$  – Incident solar irradiance [ $W/m^2$ ].

$\tau$  – Glass transmissivity.

$\alpha_s$  – Silicon absorptivity.

$U_L$  – Overall thermal losses coefficient [ $W/m^2K$ ].

$\eta_e$  – Photovoltaic conversion efficiency [%].

$N_c$  – Number of cells in the module.

$T_a$  – Ambient air temperature [K].

$T_c$  – Cells temperature [K].

To apply this model, the ambient air temperature and the wind speed should be measured, and the incident irradiance must be also known. The temperature of the covering glass (surface of the module) and backsheet (back side of the module) need to be measured for model validation.

The energy balance per unit area of a photovoltaic module in stationary regime that losses energy by heat transfer to the ambient air is given by [7]:

$$(\tau\alpha)G_t = \eta_e G_t + U_L(T_c - T_a) \quad (18)$$

According to Figure 4.2.3, the energy balance of this simplified model accounts for the existence of heat losses through convection, radiation and conduction. In the present work, the conduction losses to the environment through the support structures were not considered and, additionally, since the cell is quite thin and the heat transfer in the wafer is predominantly normal to its surface, the thermal resistance for heat conduction in the silicon was also not considered and thus its temperature was assumed as uniform. On the contrary, the heat transfer by conduction through both the cover glass and backsheet of the module are included in the model.

#### 4.2.2.1 Calculation of the overall heat transfer coefficient

According to [7], the overall thermal losses coefficient can be calculated through the following expression:

$$U_L = \frac{1}{R_{equivalent}} \quad (19)$$

In which  $R_{equivalent}$  is the equivalent thermal resistance between the silicon wafer (highest temperature) and the environment (lowest temperature).

The various thermal resistances that contribute to the overall thermal loss coefficient are examined separately next. The equivalent circuit of thermal resistances associated to each one of the heat transfer processes in the module is shown in Figure 4.2.4.

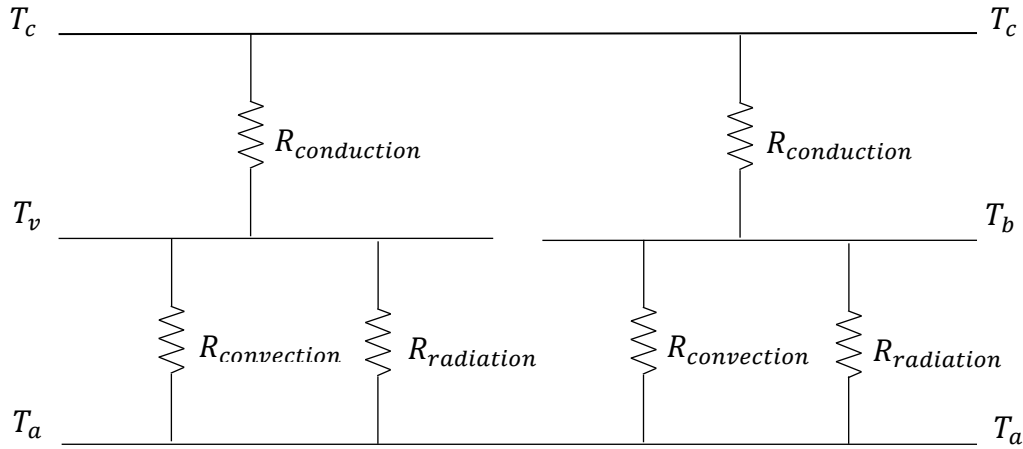


**Figure 4.2.4** - Thermal network of the solar photovoltaic module studied model, considering convection, radiation and conduction losses.

Legend of Figure 4.2.4:

$R_{conduction}$  – Conduction thermal resistance [ $m^2K/W$ ].

$R_{convection}$  – Convection thermal resistance [ $m^2K/W$ ].

$R_{radiation}$  – Radiation thermal resistance [ $m^2K/W$ ].

$T_b$  – Backsheet temperature [K].

$T_g$  – Glass temperature [K].

To calculate the equivalent resistance, first it is necessary to calculate the various heat transfer coefficients. The heat conduction processes through the glass and the backsheet are described, respectively, through the following relations [7]:

$$h_{cond,g} = \frac{k_g}{\Delta x_g} \quad (20)$$

$$h_{cond,b} = \frac{k_b}{\Delta x_b} \quad (21)$$

In which  $k_b$  and  $k_g$  are the thermal conductivities of the glass and backsheet with thicknesses  $\Delta x_b$  and  $\Delta x_g$ , respectively.

In the case of thermal radiation exchange between the glass cover and the environment and the backsheet and the environment, the following relations are respectively used [47]:

$$h_{rad,g-a} = \frac{\sigma_b(T_g^2 + T_a^2)(T_g + T_a)}{\frac{1 - \varepsilon_g}{\varepsilon_g} + \frac{1}{F_{12}} + \frac{A_m}{A_r} \left( \frac{1 - \varepsilon_r}{\varepsilon_r} \right)} \quad (22)$$

$$h_{rad,b-a} = \frac{\sigma_b(T_b^2 + T_a^2)(T_b + T_a)}{\frac{1 - \varepsilon_b}{\varepsilon_b} + \frac{1}{F_{12}} + \frac{A_m}{A_r} \left( \frac{1 - \varepsilon_r}{\varepsilon_r} \right)} \quad (23)$$

in which  $\varepsilon_g$  is the glass emissivity,  $\varepsilon_b$  is the backsheet emissivity,  $\varepsilon_r$  is the laboratorial wall emissivity and  $A_r$  is half of the laboratorial room area [ $m^2$ ] of walls, floor and roof. In the case of heat transfer by convection between glass and the environment and the backsheet and the environment, natural convection happens. The temperature is obtained by the medium temperature between the surfaces where heat transfer happens. The following relations are used [47].

$$h_{conv,g-a} = \frac{\overline{Nu}_{g-a} \times k_{air}}{L} \quad (24)$$

In which  $\overline{Nu}$  is the average Nusselt number,  $k_{air}$  is the air conductivity [ $W/mK$ ] and  $L$  is the length of the module. The average Nusselt number in a vertical wall is the addimentional total amount of heat transfer by convection and is given by the following expression [47]:

$$\overline{Nu} = 0.671 \left( \frac{Pr}{Pr + 0.986Pr^{1/2} + 0.492} \right)^{1/4} Ra^{1/4} \quad (25)$$

where,

$Pr$  – Prandtl number;

$Ra$  – Rayleigh number.

The Rayleigh number could be defined as the multiplication of the number of Grashof and the Prandtl number, as indicates the following expression [47]:

$$Ra = Gr \times Pr \quad (26)$$

In which  $Gr$  is the number of Grashof. The number of Grashof, which corresponds to the heat transfer by convection of the glass and the environment, is defined by the following equation,

$$Gr = \frac{g\beta(T_g - T_a)L^3}{\nu_c^2} \quad (27)$$

Where  $g$  is the gravitational constant [ $9.81 \text{ m/s}^2$ ] and  $\nu_c$  the kinetic viscosity [ $\text{m}^2/\text{s}$ ]. The used temperature must be evaluated at the film temperature [K] [47]:

$$T_{film_{g-a}} = \frac{(T_g + T_a)}{2} \quad (28)$$

And  $\beta$  is the volumetric coefficient of expansion [ $\text{K}^{-1}$ ]:

$$\beta = \frac{1}{T_{film_{g-a}}} \quad (29)$$

Because the  $Pr$  number depends on the air temperature, which varies in each iteration, a function of  $Pr$  number and temperature were calculated, with the help of the polyval tool of Matlab software. The fittings made are based in the table of the Appendix 7.

The most of these relations are valid for the convection between the backsheet and the ambient air. The difference is in the temperature of the film, which will modify all the relations, only because of the different temperature:

$$T_{film_{b-a}} = \frac{(T_b + T_a)}{2} \quad (30)$$

All the other quantities are made by analogous analysis. In this way, the heat transfer coefficient from backsheet to ambient air is given by the following expression,

$$h_{conv,b-a} = \frac{\overline{Nu_{b-a}} \times k_{air}}{L} \quad (31)$$

In order to calculate the glass temperature, one can use the following expression for the heat transfer through the top face of the module:

$$Q_{top} = A_m \times h_{cond\_g} \times (T_c - T_g) \quad (32)$$

and, to establish a relation with the backsheets temperature, one can use:

$$Q_{bottom} = A_m \times h_{cond\_b} \times (T_c - T_b) \quad (33)$$

The heat transfer through the external surface of the glass and the environment is described, through the following relation

$$Q_{top} = A_m \times (h_{conv,g-a} + h_{rad,g-a}) \times (T_g - T_a) \quad (34)$$

and the heat transfer through the external surface of the backsheets and the environment is described through the following relation

$$Q_{bottom} = A_m \times (h_{conv,b-a} + h_{rad,b-a}) \times (T_b - T_a) \quad (35)$$

These relations are solved through an iterative process, which starts with initial arbitrary values. The result of the iterative process is the cells temperature, the temperatures of the external surfaces of glass and backsheets and the heat transferred through the cells and the environment, simultaneously with the global energy balance (Eq. (18)).

### 4.3 Results of the experimental Nelder and Mead algorithm

This section is devoted to the validation of the Nelder and Mead algorithm, based in the experimental curve-voltage measurements. The analysis is made through the dependence that the algorithm presents regarding the values that constitute the initial simplex and the effect of the imposed tolerance.

The stopping criterion chosen to stop the iterative process is when the temperatures of the glass, backsheets and cells have a smaller difference than  $10^{-5}$  K, combined with the Nelder and Mead algorithm. Table 4.2.1 shows the initial conditions needed to start the iterative process of this integrated algorithm.

The used glass transmissivity and silicon absorptivity were combined, which resulted in a value of 0.9. The module vertical length is  $2.26 \times 10^{-1}$  m. The used room emissivity,  $\epsilon_r$ , was 0.55 and the room area that is visible by the module (walls, floor and roof) is approximately half of  $84 \text{ m}^2$ . The obtained parameters are shown in Table 4.2.2, achieved with a Nelder and Mead tolerance of  $10^{-3}$ .

**Table 4.3.1** - Initial conditions of the integrated algorithm.

Layer	Air	Glass	Cell	Backsheet
Thickness [m]	-	$5.00 \times 10^{-3}$	-	$7.00 \times 10^{-4}$
Thermal conductivity [W/mK]	Not constant	1.80	-	0.35
Emissivity	-	0.91	-	0.80
Speed [m/s]	0.1	-	-	-
Temperature [°C]	22.50	28.40	30.00	27.20
Temperature [K]	295.65	301.55	303.15	300.35

**Table 4.3.2** – Results of the estimation of the temperatures, five parameters and maximum power.

Designation	Parameter symbol	Result
Temperature of the cells	$T_c$ [°C]	42.58
Temperature of the glass	$T_g$ [°C]	42.23
Temperature of the backsheet	$T_b$ [°C]	42.57
Five parameters	$I_{ph}$ [A]	$1.75 \times 10^{-1}$
	$I_s$ [A]	$3.11 \times 10^{-12}$
	$n$	1.01
	$R_{sh}$ [Ω]	155.58
	$R_s$ [Ω]	15.54
Maximum power	$P_{mp}$ [W]	$7.13 \times 10^{-1}$

#### 4.4 Considerations

The cell temperature estimation based on measurements, which consisted on checking the minimum value of the objective function, in Figure 4.2.2, happened at 43.44°C. This means that the difference between this method and the cell temperature including the thermal analysis is about 0.86°C.

The integrated algorithm is an optimization of the pure Nelder and Mead algorithm, applied to the experiment made. Besides the temperature, the five parameters which better fit the experimental data are obtained. The key feature of this study is the extraction of the maximum

output power associated with the estimation of those parameters, that was, in this case, of  $3.01 \times 10^{-2}$  W.

Because the integrated algorithm is a coupling of a computational algorithm with a laboratorial procedure and a thermal model of the photovoltaic module, they have associated errors between them. These errors could have origin in multiple sources, namely, errors associated with the Nelder and Mead computational algorithm in the parameters estimation; uncertainties associated with the glass and backsheet temperature measurement equipment; manual reading of the glass and backsheet temperatures; conductivity and emissivity of the materials assumption values, for example, due to the presumption that the backsheet is constituted by PVD material; due to the fact of the laboratorial room isn't a controlled environment, and it has light dispersion; due to the noise of the instrumentation; or even due to the combination of some or all of those reasons.



# Chapter 5

## MPPT estimation under shadow conditions

This chapter presents the shadow identification in a photovoltaic module, validated through a laboratorial experiment. The experiment consists of acquiring the values of current and voltage, in order to obtain the I-V and P-V characteristics curves. A best-fit of the curves is done through a polynomial fitting to estimate the MPP. The main aim of this chapter is the understanding of the photovoltaic description under shadow conditions, and how the P-V curve could be simulated and optimized in order to collect the most possible power.

### 5.1 The concept of shadow and its effects on photovoltaic conversion of a module

The identification of shadows in a photovoltaic module is important to extend the modules life cycle, preventing failures of the cells and increasing the output power that can be extracted from the module. When a cell is shaded, it acts as a load, dissipating electric energy through Joule effect and, because of that, its temperature increases and generates the so-called hot spots [35], thus contributing to create an open circuit in the entire photovoltaic module [30]. To prevent this effect, bypass diodes are used [30]. The activation of bypass diodes, which provides an alternative path to the current, thus dissipating the most part of the energy generated by other unshaded cells. Although, the number of cells per bypass diode are designed to not suffer from reverse breakdown, a cell that is continuously exposed to that condition, will age faster, being more sensitive to rupture [4].

## 5.2 Analysis of characteristic curve under shaded and unshaded conditions

Photovoltaic systems are connected in series and parallel configuration, in order to increase the required power output of the array. Normally, in a series connection, the current that passes through a group of cells is the same, and the characteristic curve is obtained by the sum of the voltages measured at each cell terminals. The characteristic curve of a parallel group of cells is the sum of the current values of cells terminal, and the voltage stay constant [35]. In this work, simulated curves will be done through a polynomial fitting, being the objective the MPP determination.

### 5.2.1 Materials and methods

The used materials in this experiment were the same instruments described in Chapter 4, with the difference of the shadow object and the fact that the modules were shaded inside a black box. In this case, the used lamp source was a 70W halogen lamp. There were used two modules, the first one described in Chapter 4 (Module 1), and a smaller one (Module 2), where the measured values are described following in Table 5.2.1.

**Table 5.2.1** - Main measured characteristics of the Module 2 (small module).

<b>Characteristics of Module 2</b>	<b>Measured value</b>
Area [ $m^2$ ]	$5.2 \times 10^{-3}$
Number of cells	22
Maximum power [W]	$1.93 \times 10^{-2}$
Maximum voltage [V]	4.00
Maximum current [A]	$4.83 \times 10^{-3}$
Open circuit voltage [V]	5.29
Short circuit current [A]	$6.05 \times 10^{-3}$

### 5.2.2 Module 1 and Module 2 in unshaded conditions

Partial shadow could generate an important effect on the P-V curve of the module, visually identified as a multiple peak in the P-V curve. This is a problem as increases the difficulty of identify the MPP through an optimization algorithm. Module 1 and Module 2 were submitted

to unshaded and shaded conditions. Module 1 and Module 2 in unshaded conditions are shown in Figure 5.2.1.

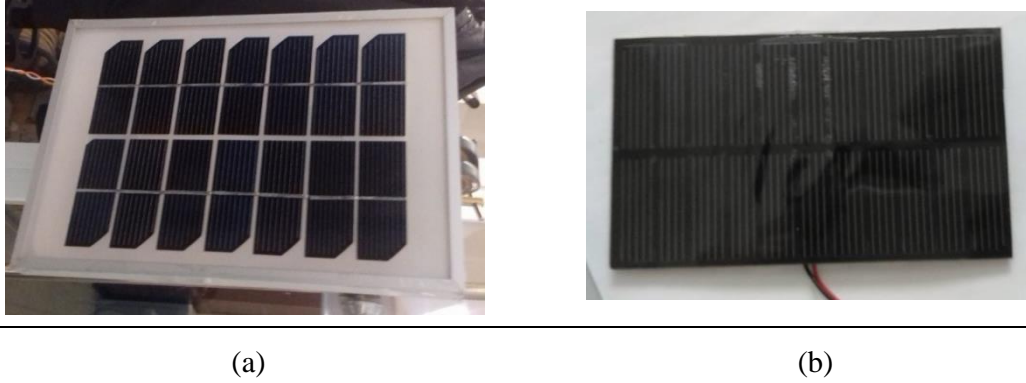


**Figure 5.2.1** - Module 1 (a) and Module 2 (b) used in the laboratorial experiments.

The correspondent I-V and P-V characteristic curves for Module 1 and Module 2 under unshaded conditions are shown in Figures 5.2.2, 5.2.3., 5.2.4, 5.3.5.

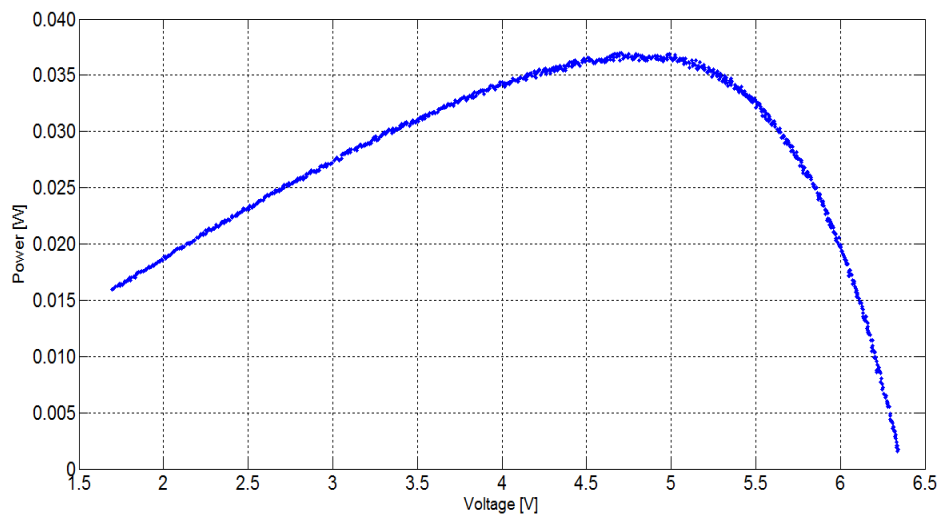


**Figure 5.2.2** - P-V curve of Module 1, measured under normal irradiation conditions.

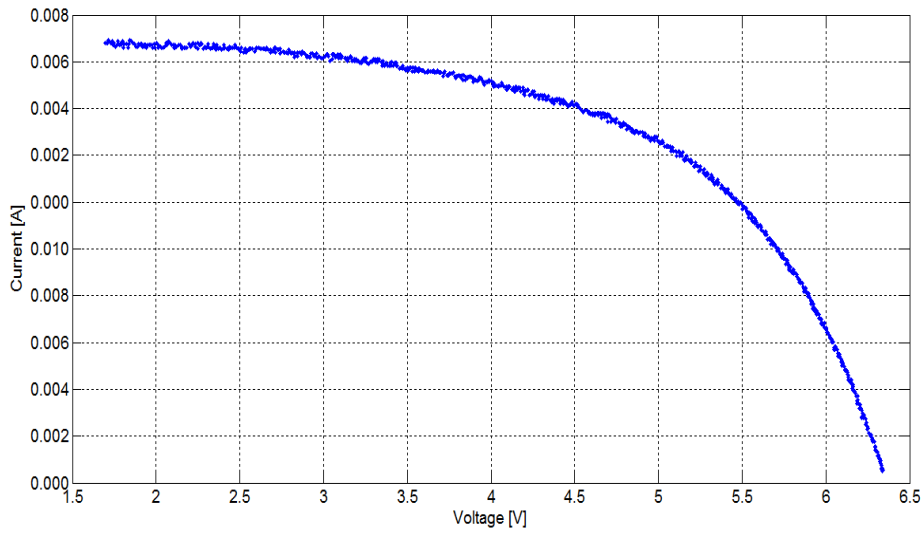


Figure 5.2.3 - I-V curve of Module 1, measured under normal irradiation conditions.

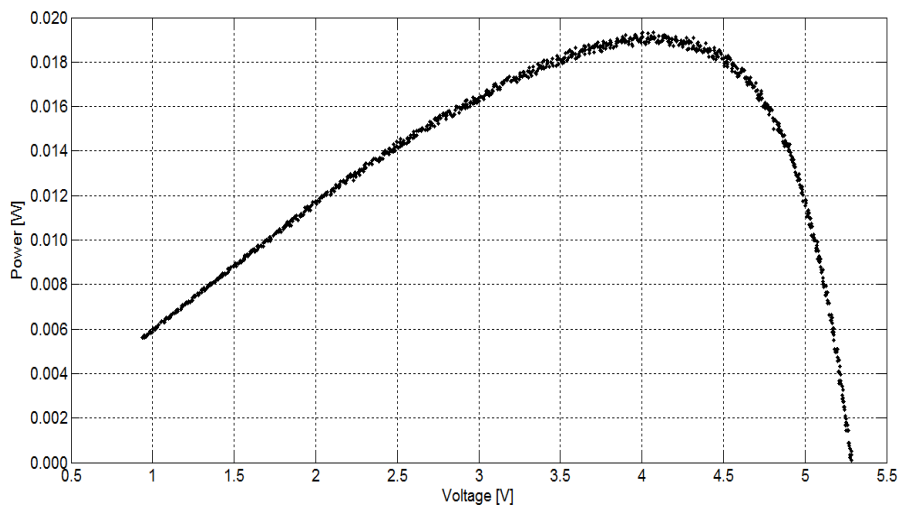


Figure 5.2.4 - Module 2 measured P-V curve under normal irradiation conditions.

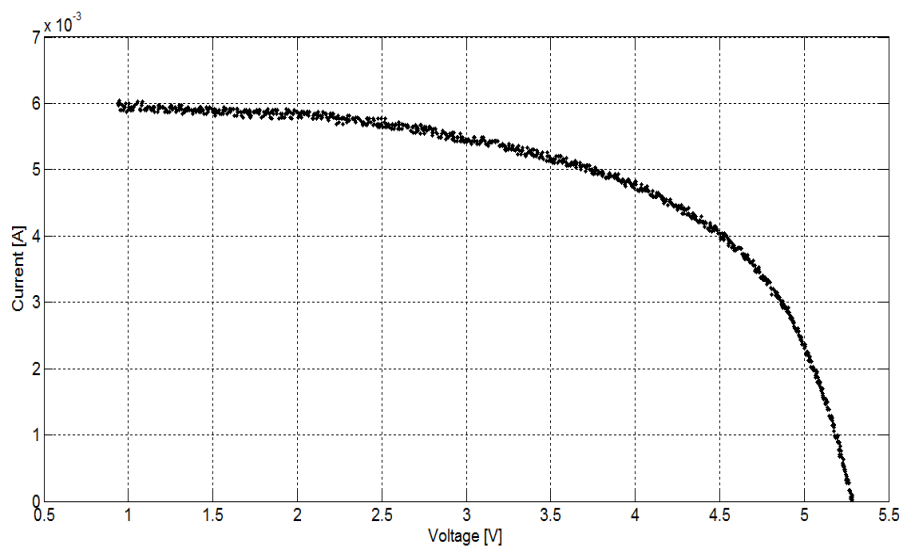
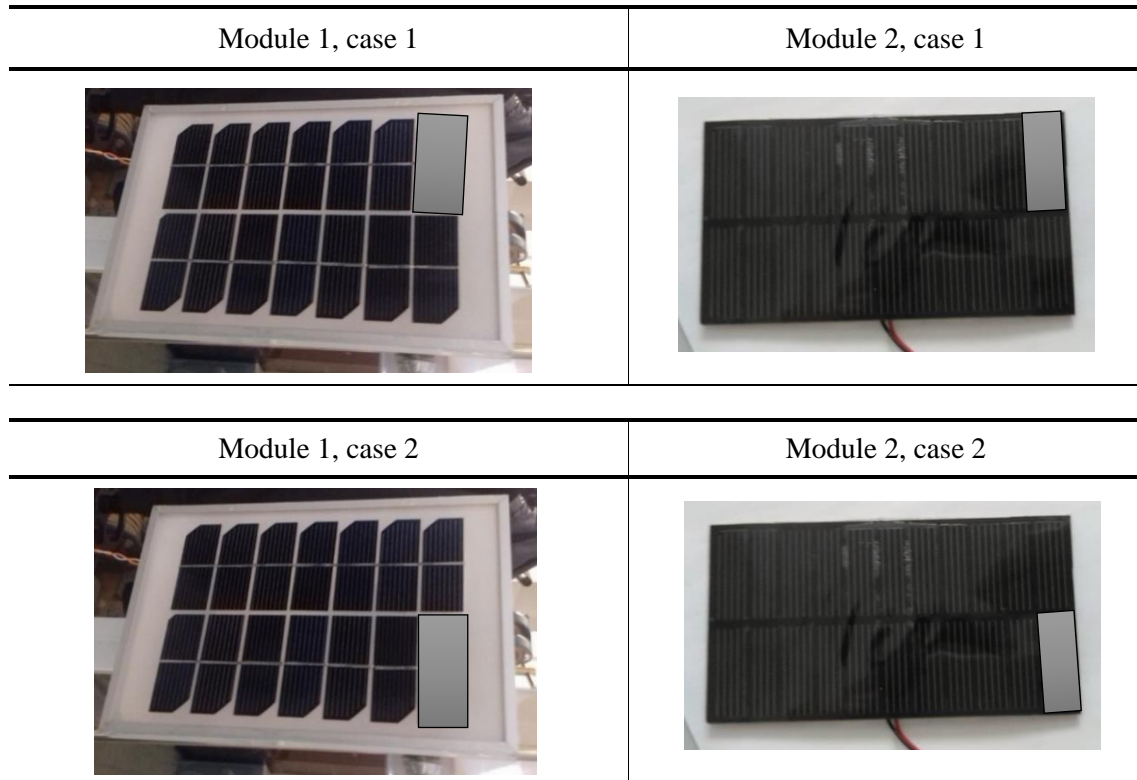


Figure 5.2.5 - Module 2 measured I-V curve under normal irradiation conditions.

### 5.2.3 Module 1 and Module 2 under shaded conditions

Module 1 and module 2 were submitted to shadow conditions. The first shaded analysis was made by covering one cell of the Module 1 and Module 2, which corresponds to case 1. The second analysis was made by covering one cell of the opposite string of the Module 1 and Module 2, which corresponds to the case 2. The configurations are presented in Figure 5.2.6.



**Figure 5.2.6** - Module 1 and Module 2 shaded cells experimental configurations – Cases of shadow 1 and 2.

After acquiring the current and voltage values, the I-V and P-V characteristic curves were constructed, under the shaded conditions presented above. The case 1 of Module 1 results are presented in Figure 5.2.7 and Figure 5.2.8, and the case 2 of Module 1 is presented in Figure 5.2.9 and Figure 5.2.10.

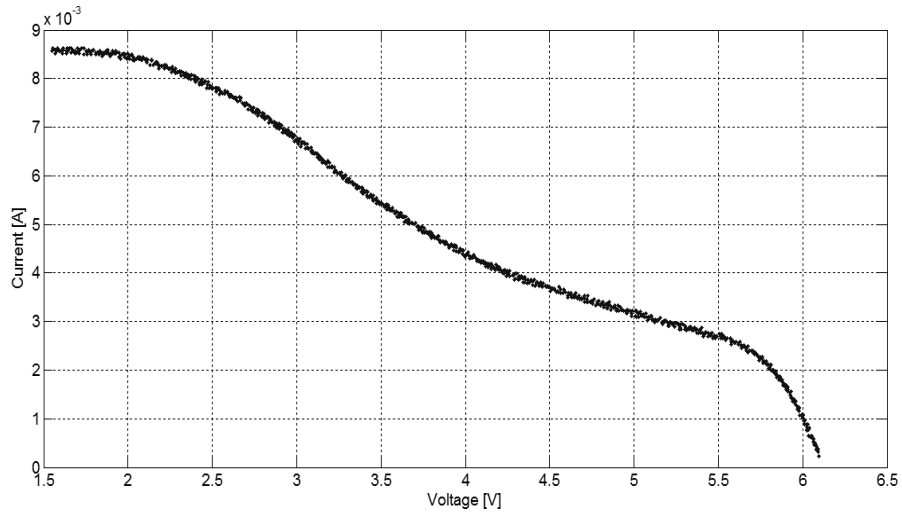


**Figure 5.2.7** - I-V curve of the Module 1, case of shadow 1.

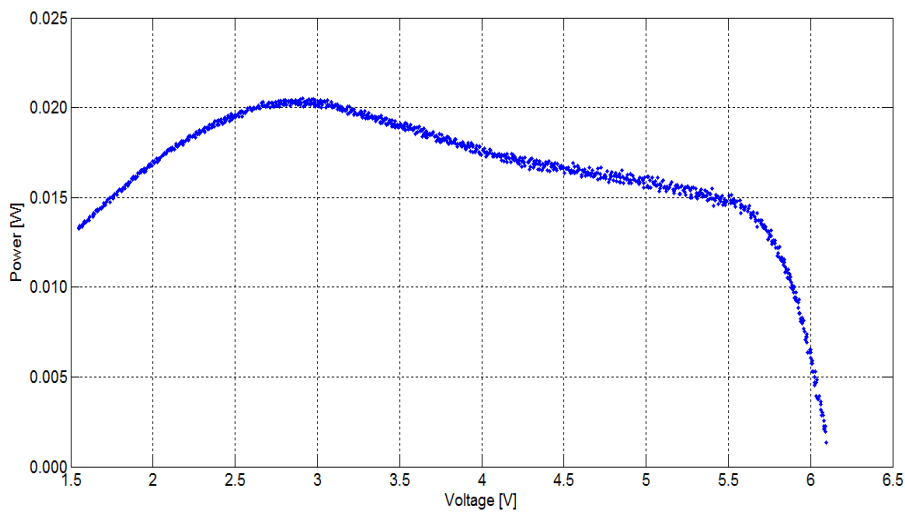


**Figure 5.2.8** - P-V curve of the Module 1, case of shadow 1.

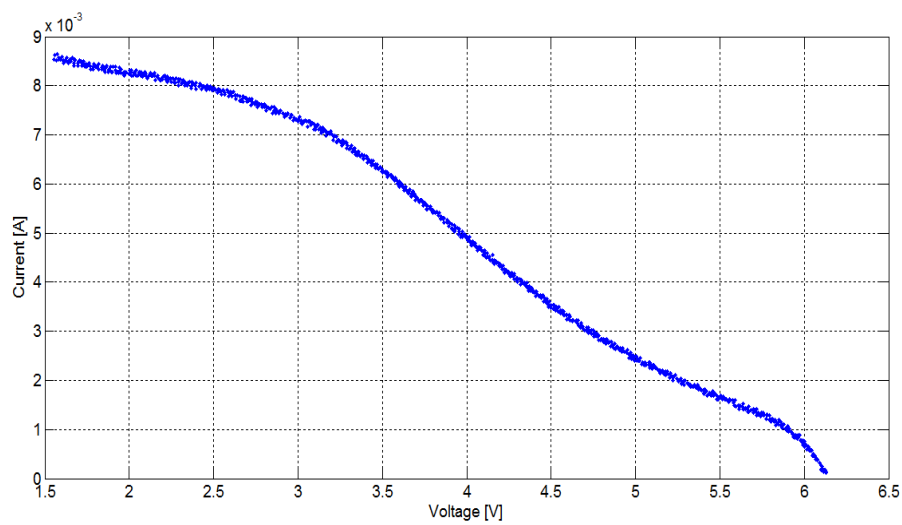


**Figure 5.2.9** - I-V curve of the Module 1, case of shadow 2.

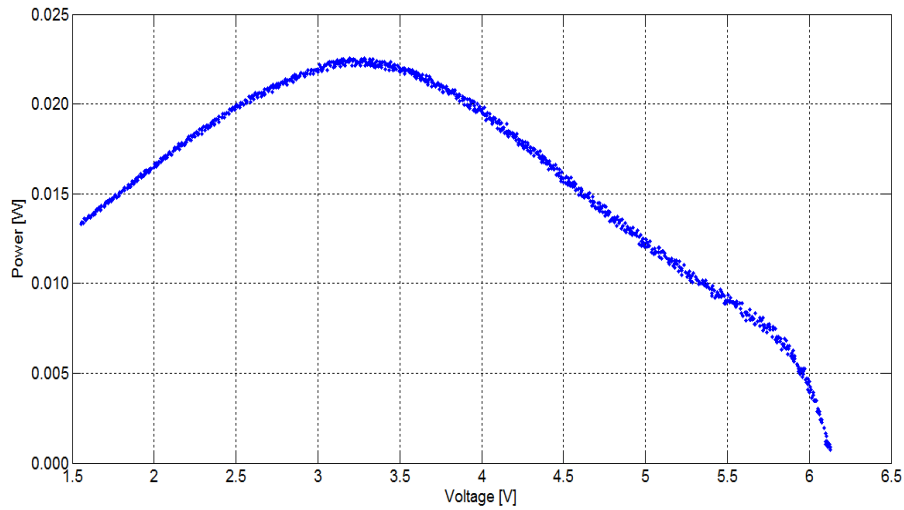


**Figure 5.2.10** - I-V curve of the Module 1, case of shadow 2.

The same procedure analysis was made to Module 2. The shadow configuration of Figure 5.2.6 was tested, in a similar way. The I-V and P-V curves of this module are presented in the following, in Figures 5.2.11, 5.2.12, 5.2.13 and 5.2.14.

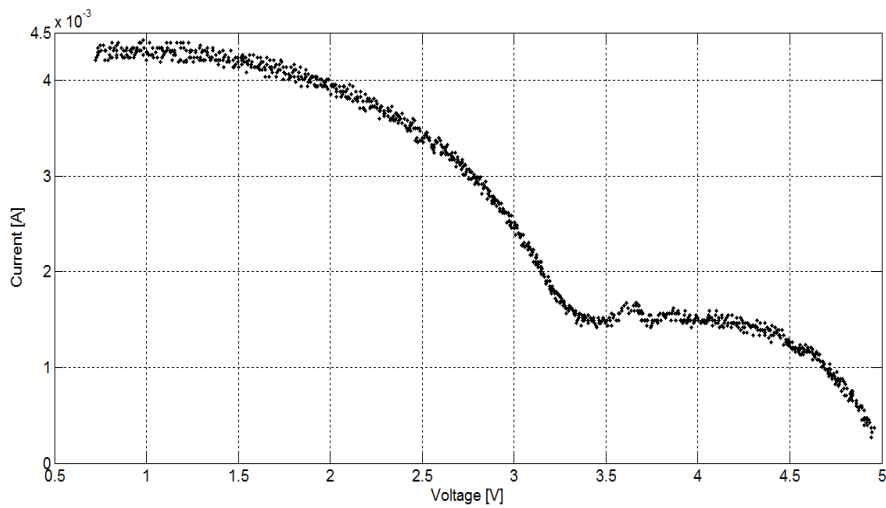


**Figure 5.2.11** - I-V curve of module 2, case of shadow 1.

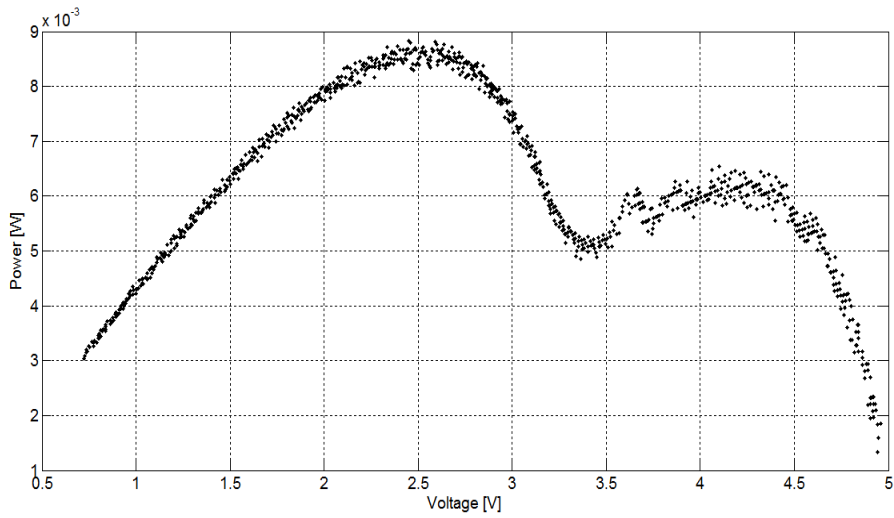


Figure 5.2.12 - P-V curve of module 2, case of shadow 1.

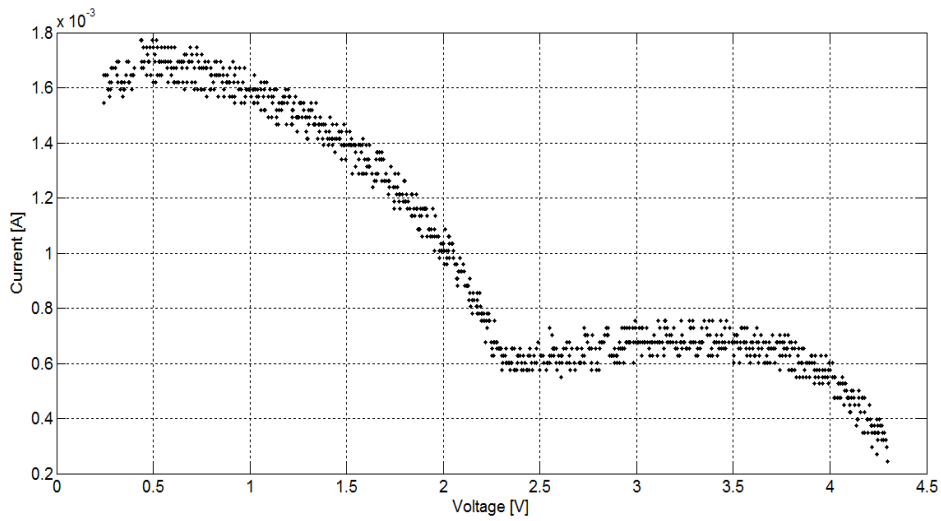


Figure 5.2.13 - I-V curve of module 2, case of shadow 2.

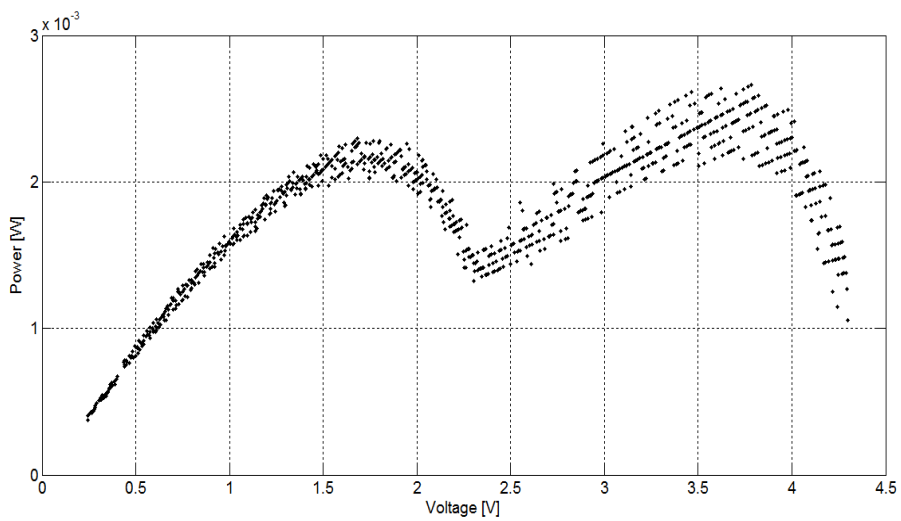


Figure 5.2.14 - P-V curve of module 2, case of shadow 2.



### 5.3 Curve fitting through polynomials

Through the traced P-V curves of Modules 1 and Module 2, one can observe the presence of local maximums. It is in those points that the MPPT shows inaccuracy, having the possibility of choosing the minor local maximum, and meaning that the maximum possible power output is not extracted.

Through a fifth and eighth degree polynomial curves the best-fits are obtained for Module 1 and Module 2, for each one of the studied cases. The local maximums are identified through the roots of the polynomials first derivatives. An example of a polynomial of the fifth degree is presented in the following equation,

$$p = C_1 \times V^5 + C_2 \times V^4 + C_3 \times V^3 + C_4 \times V^2 + C_5 \times V + C_6 \quad (36)$$

where,

$p$  – Polynomial power curve;

$C_n$  – Curve coefficients;

$V$  – Voltage value, who corresponds to the  $x$  axis [V].

Through the four performed experiments with Module 1 and Module 2 the roots of the four cases were obtained and substituted in the original polynomial. The obtained values for the power output and are presented in Table 5.3.1.

**Table 5.3.1** - Results of the calculated power values on the roots of the polynomials.

Cases	Module 1 power [W]	Module 2 power [W]
1 <sup>st</sup> case	$1.34 \times 10^{-2}$	$2.70 \times 10^{-3}$
	$2.04 \times 10^{-2}$	$8.70 \times 10^{-3}$
	$1.63 \times 10^{-2}$	$5.30 \times 10^{-3}$
	$1.63 \times 10^{-2}$	$6.40 \times 10^{-3}$
	-	$1.90 \times 10^{-3}$
2 <sup>nd</sup> case	$2.24 \times 10^{-2}$	$2.00 \times 10^{-3}$
	$1.42 \times 10^{-2}$	$1.70 \times 10^{-3}$
	-	$2.40 \times 10^{-3}$
	-	$3.15 \times 10^{-4}$

From table 5.3.1 it can be seen that the maximum power of the Module 1 case 1 is  $2.04 \times 10^{-2}$  W, which is represented in Figure 5.3.1. The Module 1 case 2 maximum power value is  $2.24 \times 10^{-2}$  W, and can be observed in Figure 5.3.2. The maximum power of Module 2 case 1 is  $8.70 \times 10^{-3}$  W, which can be seen in Figure 5.3.3. Relatively to Module 2 case 2, the maximum power value is  $2.40 \times 10^{-3}$  W, which can be observed in Figure 5.3.4.

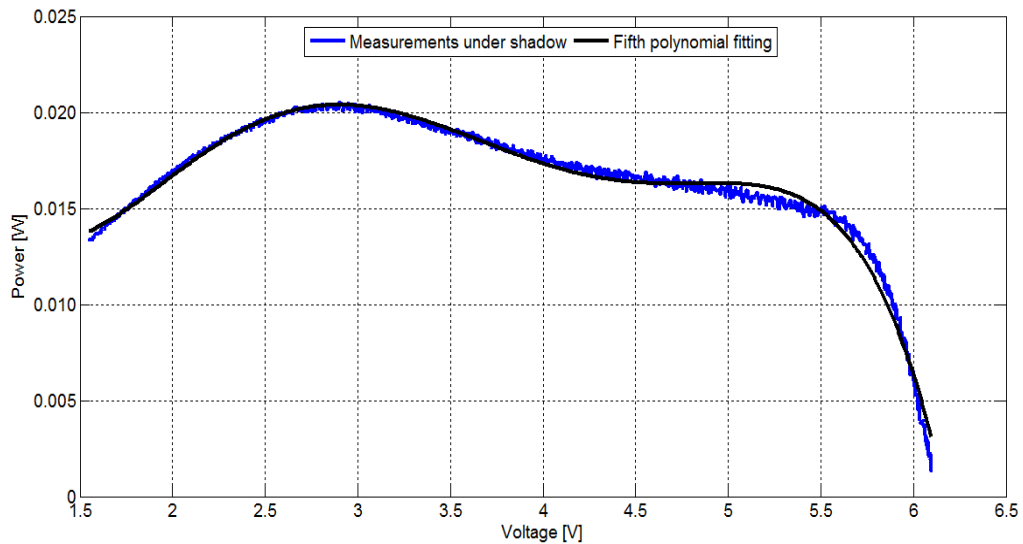


**Figure 5.3.1** - Fifth polynomial fitting with the P-V curve of module 1, case of shadow 1.

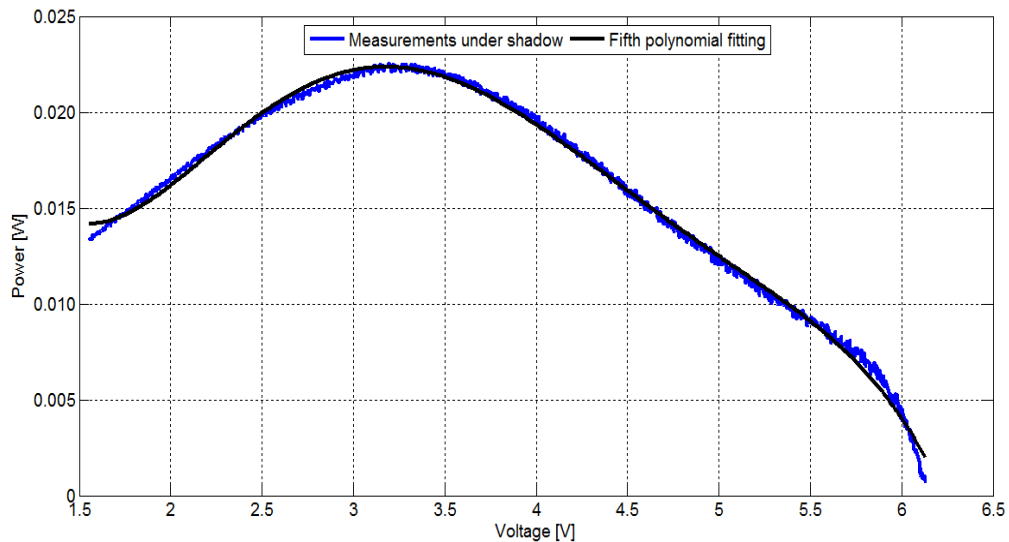


**Figure 5.3.2** - Fifth polynomial fitting with the P-V curve of module 1, case of shadow 2.

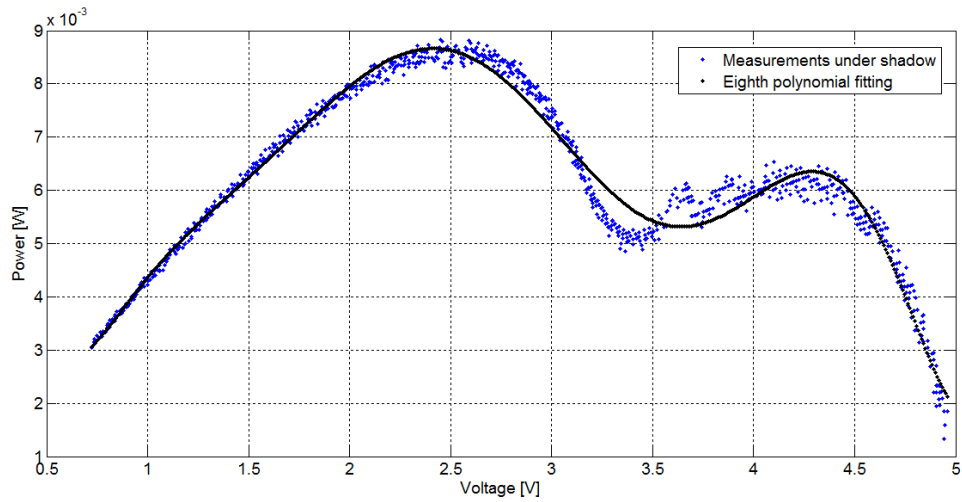


**Figure 5.3.3** - Eighth polynomial fitting with the P-V curve of module 2, case of shadow 1.

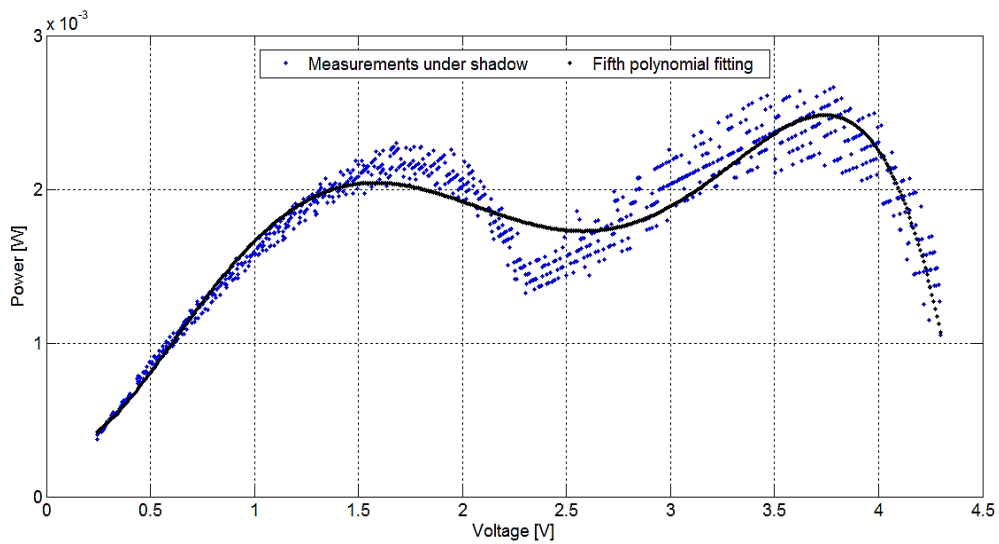


**Figure 5.3.4** - Eighth polynomial fitting with the P-V curve of module 2, case of shadow 2.

## 5.4 Considerations

The study of shadow effect on photovoltaic conversion of solar energy is extremely important to the materials life and electric energy generation.

From the laboratorial experiment that was carried out, P-V curves under shaded conditions affect the MPPT optimization.

The obtained values of Table 5.3.1 are correspondent to the obtained polynomial fitting figures. The polynomial fitting presents a satisfactory analysis in order to obtain the maximum power point of the shaded characteristic curves.

Generally, the shaded effect analysis in the overall characteristic curves consists in the connection in series of two or more modules, being one of them shaded. The presented analysis was made with just one individual module at a time, and because one detected these curves, decided to present this analysis.

Present work was an important step to understand the internal and external conditions that are responsible for this multiple MPP, and how its extraction could be made.

Because this analysis can lead us to the MPP surroundings, it would be interesting that this MPPT analysis could be a starting point of the Nelder and Mead algorithm.

# Chapter 6

## Conclusions and future work

One of this investigation main objective was the finding of a numerical efficient method for the I-V characteristic curve description, due to the fact of the correspondent equation being of non-explicit nature. This analysis lead to the study of the Bisection, Newton-Raphson and Secant numerical methods. Due to the fact of the Bisection method and the Newton-Raphson method have complementary characteristics, the coupling of these methods resulted in an optimization of the both methods.

The second aim of this dissertation was the estimation of the five parameters to make a solar cell or module description in real-time. The Nelder and Mead algorithm was constructed and validated to this aim, to validate its convergence to the known parameters, and making the description of a module based in a laboratorial experiment. The creation of an integrated algorithm for the determination of the temperature of the cell allowed a better description of the photovoltaic module, due to the fact of the convergence of the algorithm to the real parameters being directly related to this other parameter. The Nelder and Mead algorithm could be very dependent on the initial simplex constitution, and if local minimums or maximums exists, the algorithm could be stuck in these values and not extract a solution close to the real parameters. Having those considerations made, the Nelder and Mead algorithm is, in general, sufficient to make a satisfactory description of a photovoltaic cell or module by itself. However, if this method could be initially combined with another first method that could search for initial guesses closer to the order of magnitude of the real solution, the Nelder

and Mead algorithm will certainly offer convergence to the real solution, and could be considered one of the best choices to characterize photovoltaic modules.

Considering its use in the 5<sup>th</sup> dimensional space, and because it is proven that with the increase of the number of the parameters the convergence becomes limited, it should be interesting to compute the Nelder and Mead algorithm applied to the estimation of the five parameters but not the five together. Perhaps working with variables with the same order of magnitude but in a parallel approach (running at the same time), the estimation of the parameters could be optimized with this method. The temperature could be computed as a parameter, because it has a considerable impact on the determination of the parameters.

The identification of shadows was performed in a laboratorial experiment; with the aim of better understand the effect that shadow has in the photovoltaic solar modules. The identification of shaded modules is made through the analysis of the characteristic curve of the module under non-uniform irradiation, where the photo-generated current is treated as one. The main ideas that growth through this work is to insert a multiple sources introduction in the, based in the single-diode equivalent cell circuit model, to understand if that could offer a better photovoltaic cell and module description, when some of the cells are shaded. Some shade factors could be associated with those photo-generated current, and if well defined, immediately by its factor values one could quantify the module-received radiation. Another thought aspect was to explore a model of the cell which payed more attention to the temperature of the cell. Following the MPP determination, the study, improvement and implementation of the MPPT existing techniques, should lead to optimizations on the rescue the MPP task, under shaded and unshaded modules.

# Chapter 7

## References

- [1] A. K. Pandey, V. V. Tyagi, J. A. Selvaraj, N. A. Rahim and S. K. Tyagi, “Recent advances in solar photovoltaic systems for emerging trends and advanced applications,” *Renewable and Sustainable Energy Reviews*, vol. 53, p. 859–884, 2016.
- [2] L. Doman, “EIA, Independent Statistics and Analysis, US Energy Information Administration,” 2017.
- [3] D. Dimova-Malinovska, “The state-of-the-art and future development of the photovoltaic technologies - the route from crystalline to nanostructured and new emerging materials,” in *16 ISCMP: Progress in Solid State and Molecular Electronics, Ionics and Photonics*, 2010.
- [4] D. Séra, *Real-time Modeling, Diagnostics and Optimised MPPT for Residential PV systems*, Aalborg University, Institute of Energy Technology, 2009.
- [5] “Trends in Photovoltaic Applications, survey report of selected IEA countries between 1992 and 2014,” Report IEA-PVPS T1-27:2015, 2015.
- [6] SOLARGIS, “GHI Solar Map © 2017 Solargis,” [Online]. Available: <http://solargis.com/assets/graphic/free-map/GHI/Solargis-World-GHI-solar-resource-map-en.png>.
- [7] S. A. Kalagirou, *Solar Energy Engineering: Processes and Systems*, 2nd ed., New York: Elsevier, 2014.
- [8] J. T. Bialasiewicz, “Renewable Energy Systems With Photovoltaic Power Generators: Operation and Modeling,” *IEEE TRANSACTIONS ON INDUSTRIAL ELECTRONICS*, 2008.

- [9] R. K. N. Pallavee Bhatnagar, “Maximum power point tracking control techniques: State-of-the-art in photovoltaic applications,” *Renewable and Sustainable Energy Reviews* 23 (2013), pp. 224-241, 2013.
- [10] J. Khan and M. H. Arsalan, “Solar power technologies for sustainable electricity - A review,” *Renewable and Sustainable Energy Reviews*, vol. 55, pp. 414-425, 2016.
- [11] A. Cotar, A. Filcic and D. Jardas, “Photovoltaic systems,” REA Kvarner d.o.o., IRENA- Istrian regional energy agency, 2012.
- [12] U. Gangopadhyay, S. Jana and S. Das, “State of Art of Solar Photovoltaic Technology,” in *International Conference on Solar Energy*, India, 2013.
- [13] F. Blaabjerg and D. M. Ionel, “Renewable Energy Devices and Systems – State-of-the-Art,” *Electric Power Components and Systems*, vol. 43, pp. 1319-1328, 2015.
- [14] E. Rodrigues, R. Melício, V. Mendes and J. Catalão, “Simulation of a Solar Cell considering Single-Diode Equivalent Circuit Model,” *RE&PQJ*, vol. 1, 2011.
- [15] H.-L. Tsai, C.-S. Tu and Y.-J. Su, “Development of Generalized Photovoltaic Model Using Matlab/Simulink,” in *Proceedings of the World Congress on Engineering and Computer Science*, San Francisco, USA, 2008.
- [16] J. C. H. P. Daniel S. H. Chan, “Analytical Methods for the Extraction of Solar Cell Single and Double Diode Model Parameters from I-V Characteristics,” *IEEE TRANSACTIONS ON ELECTRON DEVICES*, Vols. VOL. ED-34, 1987.
- [17] Z. Chen, L. Wu, P. Lin, Y. Wu and S. Cheng, “Parameters identification of photovoltaic models using hybrid adaptive Nelder-Mead simplex algorithm based on eagle strategy,” *Applied Energy*, vol. 182, pp. 47-57, 2016.
- [18] H. Pina, Métodos Numéricos, vol. 1, Alfragide: McGRAW-HILL DE PORTUGAL, L.da, 1995.
- [19] A. A. M. T. Ana Catarina Foles, “Convergence speed optimization of iterative methods for a photovoltaic cell simulation,” in *WES Conference*, Évora, Portugal, 2016.
- [20] J. A. R. M. Nelder, “A simplex method for function minimization,” *Computer Journal*, pp. 308-313, 1965.
- [21] A. I. d. A. Correia, “Métodos de Pesquisa Directa: Optimização Não Linear,” 2010.
- [22] R. M. Lewis, V. Torczona and M. W. Trossetc, “Direct search methods: then and now,” *Journal of Computational and Applied Mathematics*, vol. 124, pp. 191-207, 2000.



- [23] W. Spendley, G. R. Hext and F. R. Himsforth, “Sequential Application of Simplex Designs in Optimisation and Evolutionary Operation,” *TECHNOMETRICS*, Vols. 4, No.4, pp. 441-461, 1962.
- [24] P. Tomislav and Z. Ban, “An Improvement of Incremental Conductance MPPT Algorithm for PV Systems based on the Nelder-Mead Optimization,” in *17th International Conference on Electrical Drives and Power Electronics – EDPE 2013*, Zagreb, Croatia, 2013.
- [25] M. R. Rashel, A. Albino, T. C. F. Goncalves and M. Tlemçani, “Sensitivity Analysis of Environmental and Internal Parameters of a Photovoltaic Cell,” in *Energy for Sustainability International Conference 2017. Designing Cities & Communities for the Future*, Funchal, Madeira, 2017.
- [26] M. R. Rashel, A. Albino, M. Tlemçani and T. C. F. Goncalves, “Sensitivity analysis of parameters of a photovoltaic cell under different conditions,” in *10th International Conference on Software, Knowledge, Information, Management & Applications*, China, 2016.
- [27] A. A. M. T. Ana Catarina Foles, “Real time characterization of a photovoltaic panel using the five parameters model,” in *AMPSECA - International Conference on Advanced Materials for Photonics, Sensing and Energy Applications*, Agadir, Morocco, 2017.
- [28] M. T. Ana Catarina Foles, “Real time characterization of a photovoltaic module considering the single diode five parameters model,” in *Workshop: Como fazer um artigo científico?*, Évora, Portugal, 2017.
- [29] M. Bressen, Y. E. Basri, A. Galeano and C. Alonso, “A shadow fault detection method based on the standard error analysis of I-V curves,” *Renewable Energy*, vol. 99, pp. 1181-1190, 2016.
- [30] M. Seyedmahmoudian, S. Mekhilef, R. Rahmani, R. Yusof and E. T. Renani, “Analytical Modeling of Partially Shaded Photovoltaic Systems,” *Energies*, vol. 6, pp. 128-144, 2013.
- [31] H. A. Kazem, M. T. Chaichan, A. H. Alwaeli and K. Mani, “Effect of Shadow on the Performance of Solar Photovoltaic,” in *Mediterranean Green Buildings & Renewable Energy*, pp., 2017.
- [32] J. P. Ram and N. Rajasekar, “A new global maximum power point tracking technique for solar photovoltaic (PV) system under partial shading conditions (PSC),” *Energy*, vol. 118, pp. 512-525, 2017.
- [33] V. Khanna, B. Das, D. Bisht, Vandana and P. Singh, “A three diode model for industrial solar cells and estimation of solar cell parameters using PSO algorithm,” *Renewable Energy*, vol. 78, pp. 105-113, 2015.

- [34] Y.-J. Wang and P.-C. Hsu, “Analysis of Partially Shaded PV Modules Using Piecewise Linear Parallel Branches Model,” vol. 36, 2009.
- [35] R. Pereira, R. Melicio, V. Mendes and A. Joyce, “PV System with Maximum Power Point Tracking: Modeling, Simulation and Experimental Results,” in *Conference on Electronics, Telecommunications and Computers - CETC 2013*, 2014.
- [36] R. Jovanovica, S. Kaisa and F. H. Alharbia, “Cuckoo Search Inspired Hybridization of the Nelder-Mead Simplex Algorithm Applied to Optimization of Photovoltaic Cells,” *Applied Mathematics & Information Sciences*, vol. 3, pp. 961-973, 2016.
- [37] NREL, “NREL - System Advisor Model,” [Online]. Available: <https://sam.nrel.gov/>.
- [38] M. Baptista, “Sistemas de aquisição de dados”.
- [39] N. Instruments, “Low-Cost, Bus-Powered Multifunction DAQ for USB 12- or 14-Bit, Up to 48 kS/s, 8 Analog Inputs,” [Online]. Available: <http://www.ni.com/datasheet/pdf/en/ds-218>.
- [40] Tektronix, “Arbitrary Function Generators AFG310 AFG320,” [Online]. Available: [http://www.tek.com/sites/tek.com/files/media/media/resources/76W\\_12019\\_4.pdf](http://www.tek.com/sites/tek.com/files/media/media/resources/76W_12019_4.pdf).
- [41] N. Instruments, “NI GPIB-USB-HS,” [Online]. Available: <http://www.ni.com/datasheet/pdf/en/ds-264>.
- [42] OSRAM, “HALOLINE 1000 W 230 V R7S,” [Online]. Available: <http://docs-europe.electrocomponents.com/webdocs/1374/0900766b81374da8.pdf>.
- [43] VAISALA, “Vaisala Weather Transmitter WXT530 Series,” [Online]. Available: [http://www.vaisala.com/Vaisala%20Documents/Brochures%20and%20Datasheets/WEA-MET-G-WXT530%20Datasheet\\_\\_Low.pdf](http://www.vaisala.com/Vaisala%20Documents/Brochures%20and%20Datasheets/WEA-MET-G-WXT530%20Datasheet__Low.pdf).
- [44] LEYBOLD, “Digital Thermometer (666 209),” [Online]. Available: <https://www.ld-didactic.de/documents/en-US/GA/GA/6/666/666209e.pdf>.
- [45] LEYBOLD, “Temperature Sensor NiCr-Ni,” [Online]. Available: <https://advlabwiki.johnshopkins.edu/images/666193DE.pdf>.
- [46] M. F. Santos, “Balanço Energético de um Módulo Fotovoltaico, Algumas Aplicações,” 1995.
- [47] A. Bejan, *Transferência de Calor*, Edgard Blucher Ltda, 1996.

# Chapter 8

## Appendix

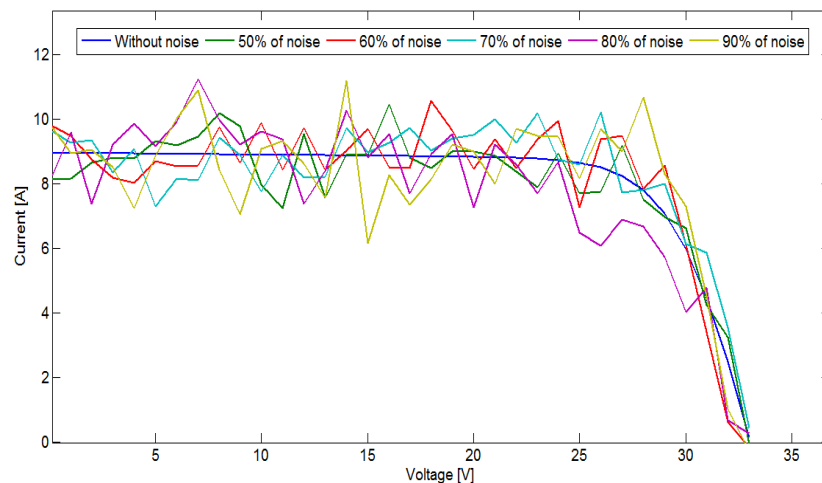
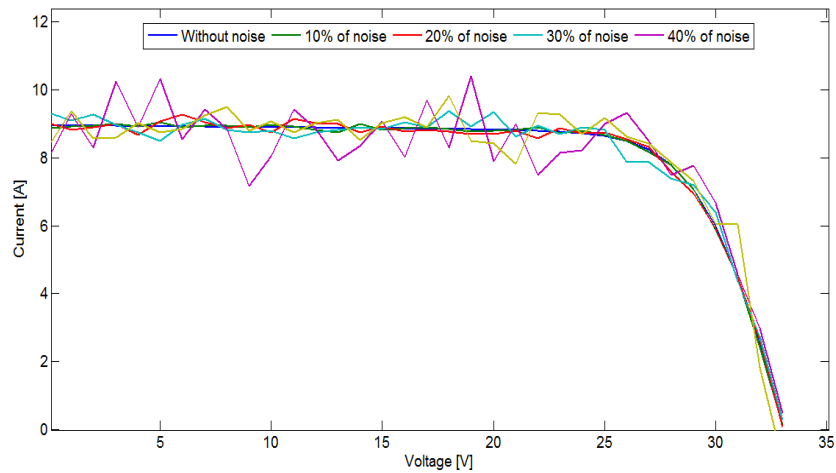
**APPENDIX 1** – Initial conditions of the Nelder and Mead algorithm: maximum relative difference from the assumed NREL values of 10, 30, 50, 70 and 90%.

10%						
Parameter	$P_1$	$P_2$	$P_3$	$P_4$	$P_5$	$P_6$
$I_{ph}$ [A]	9.768	9.857	9.588	9.499	9.679	9.633
$I_s$ [ $\times 10^{-9}$ A]	3.920	3.880	4.010	4.051	3.970	3.992
$n$	1.308	1.320	1.284	1.272	1.296	1.290
$R_{sh}$ [ $\Omega$ ]	153.74	152.06	157.12	158.12	155.43	156.28
$R_s$ [ $\Omega$ ]	0.1966	0.1944	0.2009	0.2030	0.1987	0.1998
30%						
$I_{ph}$ [A]	10.753	10.574	11.470	10.305	11.649	11.201
$I_s$ [ $\times 10^{-9}$ A]	3.448	3.534	4.103	3.664	3.017	3.233
$n$	1.440	1.416	1.536	1.380	1.560	1.500
$R_{sh}$ [ $\Omega$ ]	153.746	152.069	157.121	158.128	155.435	156.283
$R_s$ [ $\Omega$ ]	0.197	0.194	0.201	0.203	0.199	0.200
50%						
$I_{ph}$ [A]	11.649	13.262	12.545	13.442	12.994	12.097
$I_s$ [ $\times 10^{-9}$ A]	3.021	2.245	2.593	2.161	2.373	2.804
$n$	1.56	1.776	1.680	1.803	1.741	1.620
$R_{sh}$ [ $\Omega$ ]	118.265	87.854	101.370	84.475	92.923	109.818
$R_s$ [ $\Omega$ ]	0.151	0.112	0.129	0.108	0.119	0.140

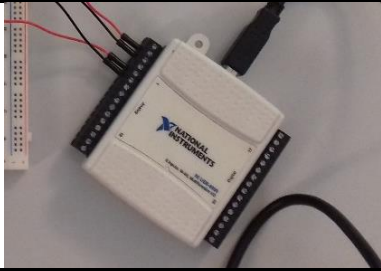
70%						
$I_{ph}$ [A]	15.054	14.786	13.890	13.442	15.234	14.338
$I_s$ [ $\times 10^{-9}$ A]	1.379	1.509	1.940	2.156	1.293	1.724
$n$	2.016	1.980	1.860	1.801	2.040	1.921
$R_{sh}$ [ $\Omega$ ]	54.064	59.133	76.028	84.475	50.685	67.580
$R_s$ [ $\Omega$ ]	0.069	0.076	0.097	0.108	0.065	0.086
90%						
$I_{ph}$ [A]	17.023	16.578	16.130	15.234	15.682	14.338
$I_s$ [ $\times 10^{-9}$ A]	4,288	6.473	8.621	1.290	1.082	1.721
$n$	2.281	2.221	2.162	2.045	2.100	1.915
$R_{sh}$ [ $\Omega$ ]	16.895	25.343	33.790	50.685	42.238	67.580
$R_s$ [ $\Omega$ ]	0.022	0.032	0.043	0.065	0.054	0.086

Note:  $P_1, P_2, P_3, P_4, P_5$  and  $P_6$  are the vertices which compose the simplex.


**APPENDIX 2 - Imposed current value of noise, using the Newton-Raphson method.**




**APPENDIX 3 – Data acquisition board characteristics [39].**


<b>Image of the instrument</b>		
<b>Analog Inputs</b>		
Analog inputs		8 single-ended, 4 differentials, software selectable
Input resolution		14 bit differential, 13 bit single-ended
Max sampling rate		48 kS/s
Input range	Single-ended	$\pm 10\text{ V}$
	Differential	$\pm 20\text{ V}$ , $\pm 10\text{ V}$ , $\pm 5\text{ V}$ , $\pm 4\text{ V}$ , $\pm 2.5\text{ V}$ , $\pm 2\text{ V}$ , $\pm 1.25\text{ V}$ , $\pm 1\text{ V}$
Working voltage		
Input impedance		
Overvoltage protection		
System noise	Single-ended	$\pm 10\text{ V}$ range; 5mVrms
	Differential	$\pm 20\text{ V}$ range; 5mVrms; $\pm 1\text{ V}$ range; 0,5mVrms
<b>Analog Outputs</b>		
Analog Outputs		2
Output resolution		12 bits
Output range		0 to +5 V
Short circuit current		50 mA
<b>Digital I/O</b>		
Absolute maximum voltage range		-0,5 to 5,8 V with respect to GND
Output driver type		Each channel individually programmable as active drive (push-pull) or open collector (open-drain)
Resolution		32 bits

**APPENDIX 4 – Function Generator and GPIB characteristics [41].**

<b>Image of the GPIB instrument</b>		
<b>Performance</b>		
Three wire		Up to 1800 Kbytes/s
HS488		Up to 7820 Kbytes/s
<b>Power Requirements</b>		
GPIB-USB Interfaces		Bus Power @ 500 mA max


<b>Image of the Function Generator instrument</b>	
Output channels	2
Standard waveforms	Sine, square, triangle, ramp, pulse, DC, noise
<b>Output characteristics</b>	
Amplitude (into 50Ω)	50mV <sub>p-p</sub> to 10mV <sub>p-p</sub> . Accuracy: ±(1% of setting + 5mV) at 1kHz, no offset
Offset (into 50Ω)	505 mV <sub>p-p</sub> to 10 V <sub>p-p</sub> amplitude: peak amplitude + offset is limited to +5V or -5 V. 50 mV <sub>p-p</sub> to 500 mV <sub>p-p</sub> amplitude: -0.75 V to +0.75 V. Accuracy: ± (1% of setting +5 mV)
Resolution	5 mV
Impedance	50Ω

**APPENDIX 5 – Air temperature and wind speed sensor characteristics [43].**

<b>Image of the Vaisala instrument</b>	
<b>Wind speed</b>	
Range	0-60 m/s
Response time	0,25 s
Available variables	Average, maximum and minimum
Accuracy	±3 % at 10m/s
Output resolution	0,1 m/s (km/h, mph, knots)
<b>Air Temperature</b>	
Range	-52 ... +60°C (-60 ... +140°F)
Accuracy (for sensor element)	At +20°C(+68°F) ±0,3°C (0,17°F)

Output resolution	0,1 °C (0,1°F)
-------------------	----------------

**APPENDIX 6** – Digital thermometer [44] and temperature probe (sensor) [45].

<b>Digital Thermometer</b>	
<b>Image of the instrument</b>	
Display	4 1/2-digit red LED display
Measuring range	$N_iC_r - N_i$ : -200 ... + 1200 °C NTC: -20 ... + 120 °C
Resolution	-200 ... + 1200 °C: 0,1 K or 0,01 K
Accuracy	0,2 °C resp. 0,2 % of measured value
Data bits	8
Analog output	12-bit conversion switchable resolution 1 °C = 1 mV = 10 mV output voltage max. ± 3V user-definable switching point
Supply voltage	12 V AC/580 mA, via plug-in supply unit
<b>Temperature Sensor <math>N_iC_r - N_i</math></b>	
Thermocouple	$N_iC_r - N_i$
Sensitivity	Approximated 41 μV/°C
Temperature range	-200 °C ... + 400 °C
Response time (99% of end value)	0.8 s in liquids, >15s in gases
Measuring sensor	non-insulated
Tolerance Class	40 °C ... 335 °C: ± 2.5 °C 335 °C ... 400 °C: ± 0.75% of measured temperature

---

**APPENDIX 7** – Air temperature as a function of the kinetic velocity, conductivity and Pr number of the air [7].

<b>T [K]</b>	<b><math>v_c</math> [<math>m^2/s</math>]</b>	<b><math>k_{air}</math> [W/mK]</b>	<b><i>Pr</i></b>
100	$1.923 \times 10^{-6}$	0.00925	0.770
150	$4.343 \times 10^{-6}$	0.01374	0.753
200	$7.490 \times 10^{-6}$	0.01809	0.739
250	$9.490 \times 10^{-6}$	0.02227	0.722
300	$1.684 \times 10^{-5}$	0.02624	0.708
350	$2.076 \times 10^{-5}$	0.03003	0.697
400	$2.590 \times 10^{-5}$	0.03365	0.689
450	$3.171 \times 10^{-5}$	0.03707	0.683
500	$3.790 \times 10^{-5}$	0.04038	0.680
550	$4.434 \times 10^{-5}$	0.04360	0.680
600	$5.134 \times 10^{-5}$	0.04659	0.680
650	$5.851 \times 10^{-5}$	0.04953	0.682
700	$6.625 \times 10^{-5}$	0.05230	0.684